CLS
COLLECTE LOCALISATION SATELLITES

Consortium Members

TU Delft Delft University of Technology
SATOC Satellite Oceanographic Consultants
DTU Space National Space Institute
isardSAT
National Oceanography Centre Natural Environment Research Council
NOVELTIS
Starlab Living Science
U.PORTO Faculdade de Ciências Universidade do Porto

ESA Cryosat Plus for Oceans

Validation Report: WP5000 Assessment of RDSAR solution (RADS) for Open Ocean

Reference: CLS-DOS-NT-14-086
Nomenclature: CP4O-WP5000-VR-08
Issue: 2. 0
Date: Oct. 13, 14

esa European Space Agency

cnes CENTRE NATIONAL D'ÉTUDES SPATIALES

Chronology Issues:			
Issue:	Date:	Reason for change:	Author
1.0	10/09/14	Creation of Issue 1.0 document	M. Raynal T. Moreau
2.0	13/10/14	Incorporated all changes and comments provided	D. Cotton

People involved in this issue:		
Written by (*):	M. Raynal (CLS) T. Moreau (CLS)	Date + Initials:(visa or ref)
Checked by (*):	R. Scharroo (Eumetsat) S. Labroue (CLS)	Date + Initial:(visa ou ref)
Approved by (*):	F. Boy (CNES)	Date + Initial:(visa ou ref)
Application authorized by (*):	(ESA) N. Picot (CNES)	Date + Initial:(visa ou ref)

**In the opposite box: Last and First name of the person + company if different from CLS*

Index Sheet:	
Context:	
Keywords:	[Mots clés]
Hyperlink:	

Distribution:		
Company	Means of distribution	Names
CLS	Notification	

List of tables and figures

List of tables:

Aucune entrée de table d'illustration n'a été trouvée.
Dans le document, sélectionnez les mots à inclure dans la table des matières, puis, sur l'onglet Accueil, sous Styles, cliquez sur un style d'en-tête. Répétez l'opération pour chaque en-tête à inclure, puis insérez la table des matières dans le document. Pour créer manuellement une table des matières, sur l'onglet Éléments de document, sous Table des matières, pointez sur un style, puis cliquez sur la flèche vers le bas. Cliquez sur un des styles sous Table des matières manuelle, puis tapez les entrées manuellement.

List of figures:

Figure 1: The mode mask, uploaded to CryoSat-2 in July 2012 (left panel) and January 2013 (right panel) (from *http://cryosat.mssl.ucl.ac.uk/qa/mode.php*) with the selected box areas. . 2

Figure 2: Mean misfit curve for v13 CPP (plotted in yellow) and TUDelft solution (plotted in red) as function of SWH in July 2012 (left panel) and January 2013 (right panel). 6

Figure 3: Map of misfit difference in January 2013 for ascending passes 6

Figure 4: Mean SLA spectrum for v13 CPP (plotted in blue) and TUDelft solution (plotted in red) in January 2013 over the entire SAR-mode area. The abscissa represents the wavelengths (on the top of the plot) or equivalently the wavenumbers (1/km). 7

Figure 5: Differences of SLA from TUDelft RDSAR solution and V13 CPP dataset as function of the latitude for one pass located in the Pacific box. Differences plotted at 20-Hz in blue and averaged differences per band of latitudes in red. 8

Figure 6: Differences of 20-Hz (in blue) tracker range (upper left panel), estimated epoch (upper right panel) and orbit corrected from time tag bias (bottom panel) from TUDelft RDSAR solution and V13 CPP dataset as function of latitude for one pass located in the Pacific box, and averaged differences per band of latitudes (in red)..... 9

Figure 7: Histogram of 20-Hz SLA for the ESRIN SAR solution (in red) and V13 CPP (in blue) in January 2013 (ascending passes)..... 9

Figure 8: Differences of SLA (left panel) and range altimeter (right panel) from TUDelft solution and V13 CPP dataset as function of filtered SWH over two months (July 2012 and January 2013)..... 10

Figure 9: SLA computed on ascending and descending passes in the Pacific box for both solutions as function of band of latitudes..... 10

Figure 10: Dependencies of 20-Hz range residual with filtered SWH and radial velocity for ascending (left panel) and descending passes (right panel) in July 2012. 11

Figure 11: 20-Hz corrected orbit residual in function of radial velocity for ascending and descending passes in July 2012. 11

Figure 12: Differences of SLA from TUDelft solution and V13 CPP dataset as function of the latitude for ascending (black curve) and descending (red curve) passes in the Pacific and North East Atlantic boxes in July 2012. .. 12

Figure 13: Differences of SLA from TUDelft solution and V13 CPP dataset as function of the radial velocity for ascending (black curve) and descending (red curve) passes in the Pacific and North East Atlantic boxes in July 2012..... 12

Figure 14: Difference of SLA from TUDelft RDSAR solution and V13 CPP for ascending (left panel) and descending passes (right panel) in July 2012. . 13

Figure 15: Map of the radial velocity values for ascending passes (left panel) and descending passes (right panel) in July 2012 13

Figure 16: TUDelft RDSAR solution (in red) and V13 CPP (in blue) SLA profiles in July 2012 over the North East Atlantic area. Shaded region corresponds to land. 14

Figure 17: SLA statistics (mean, number of points, standard deviation) as function of the distance to the coast by using the TUDelft RDSAR solution (in blue) and V13 CPP (in red) retrackers in ascending (left panel) and descending (right panel) passes. 14

Figure 18: Difference of range between the two different versions of CPP: before (v13) and after (v14) correcting the one-gate shifted waveform error. 15

Figure 19: SLA plot of TUDelft solution and V14 CPP dataset (right panel) as function of filtered SWH, and their differences (left panel) as function of band of latitudes over two months. 16

Figure 20: Corrected differences of SLA from TUDelft solution and V14 CPP dataset as function of filtered SWH over two months (July 2012 and January 2013)..... 16

Figure 21: Mean differences of SLA (left) between ascending and descending passes as function of band of latitudes for the TUDelft solution (in green) and the V14 CPP dataset (in blue) over two months (July 2012 and January 2013). Mean differences of SLA after timing bias correction of -541us applied on TUDelft data sets (right)..... 17

Figure 22: Mean SLA as function of band of latitudes for the TUDelft solution (in red), the V14 CPP dataset (in green) and the CPP LRM (in blue) over two months (July 2012 and January 2013). 17

Figure 23: Mean SLA as function of band of latitudes for the TUDelft solution corrected of -541us timing bias (in red), the V14 CPP dataset (in green) and the CPP LRM (in blue) over two months (July 2012 and January 2013).18

Figure 24: Mean SWH spectrum for V13 CPP (plotted in blue) and TUDelft solution (plotted in red) in January 2013 over the entire SAR-mode area.

The abscissa represents the wavelengths (on the top of the plot) or equivalently the wavenumbers (1/km). 19
Figure 25: Histogram of 20-Hz SWH from TUDelft RDSAR solution (in red) and V13 CPP (in red) in July 2012. 19
Figure 26: Dependencies of 20-Hz SWH residual with filtered SWH, in July 2012 (left panel) and January 2013 (right panel). 20
Figure 27: Dependencies of 20-Hz SWH residual with filtered SWH and radial velocity in Jan 2013 for ascending (left panel) and descending (right panel) passes. 20
Figure 28: Difference of SWH between TUDelft and V13 CPP (top panel) and map of SWH in July 2012 (bottom panel) for descending passes. 21
Figure 29: Difference of SWH between TUDelft and V13 CPP (top panel) and map of SWH in January 2013 (bottom panel) for ascending passes..... 22
Figure 30: Dependencies of 20-Hz SWH residual with filtered SWH between V13 CPP and V14 CPP, in July 2012 (left) and January 2013 (right). 23
Figure 31: 20-Hz SWH residual between TUDelft and V14 CPP solutions as function of filtered SWH, for ascending and descending passes..... 23
Figure 32: Mean SWH as function of band of latitudes for the TUDelft solution (in red), the V14 CPP dataset (in green) and the CPP LRM (in blue) over two months (July 2012 and January 2013). 24
Figure 33: Mean sigma0 spectrum for V13 CPP (in blue) and TUDelft solution (in red) in January 2013 over the entire SAR-mode area..... 24
Figure 34: Histogram of 20-Hz Sigma0 from TUDelft RDSAR solution and V13 CPP in January 2013 for ascending (left panel) and descending (right panel) passes. 25
Figure 35: Dependencies of 20-Hz sigma0 residual with filtered SWH, in July 2012 and January 2013. 25
Figure 36: Dependencies of 20-Hz sigma0 residual (in dB unit) with filtered SWH and radial velocity in January 2013 for ascending (left panel) and descending (right panel) passes. 26
Figure 37: Difference of sigma0 from TUDelft RDSAR solution and CPP (top panel), and maps of SWH differences, in January 2013 for ascending passes. 27
Figure 38: Mean sigma0 as function of band of latitudes for the TUDelft solution (in red), the V14 CPP dataset (in green) and the CPP LRM (in blue) over two months (July 2012 and January 2013). 27
Figure 39: Mean map of difference of square-mispointing angle from TUDelft RDSAR solution and v13 CPP for ascending (left panel) and descending passes (right panel) in January 2013..... 28
Figure 40: Mean square-mispointing angle as function of band of latitudes for the TUDelft solution (in red), the V13 CPP dataset (in green) and the CPP LRM (in blue) over July 2012 and January 2013..... 28

Figure 41: Mean square-mispointing angle as function of band of latitudes for the TUDelft solution (in red), the V14 CPP dataset (in green) and the CPP LRM (in blue) over two months (July 2012 and January 2013). 29

Figure 42: Mean map of difference of squared antenna-mispointing angle from V14 CPP product and the star trackers for ascending (left panel) and descending passes (right panel) in July 2012. 30

Applicable documents

Reference documents

RD 1 Manuel du processus Documentation
CLS-DOC

Acronyms List

AGC	Automatic Gain Control
CLS	Collecte Localisation Satellite
CPP	Cryosat Processing Prototype
ESA	European Space Agency
ESRIN	European Space Research Institute
IPF	Instrument Processing Facility
LPF	Low-Pass Filter
LRM	Low Resolution Mode
NA	Not Applicable
MQE	Mean Quadratic Error
PLRM	Pseudo - Low Resolution Mode
PTR	Point Target Response
RADS	Radar Altimeter Database System
RD	Reference Document
RDSAR	Reduced Synthetic Aperture radar
SAMOSA	SAR Altimetry MOde Studies and Applications
SAR	Synthetic Aperture radar
SIRAL	Synthetic Aperture Interferometric Radar Altimeter
SLA	Sea level Anomalies
SSH	Sea Surface Height
SWH	Significant Wave Height
TUDelft	Delft Technical University

List of Contents

1. Introduction 1
1.1. Purpose and scope 1
1.2. Document structure 1
2. Data and method overview 2
2.1. Data coverage and period 2
2.2. Method description 3
2.2.1. RADS RDSAR solution (TUDelft) 3
2.2.2. CPP RDSAR solution 3
2.2.3. Discrepancies 3
2.2.4. Edited data 4
3. Validation results and overall assessment 5
3.1. Performances of the waveform fitting 5
3.1.1. Misfit analysis 5
3.2. Comparison of range estimates 6
3.2.1. Spectral analysis of the SLA 7
3.2.2. SLA Histogram 9
3.2.3. Dependencies between parameters 10
3.2.3.1. Dependency on wave height 10
3.2.3.2. Dependency on radial velocity 11
3.2.4. SLA cartography 13
3.2.5. SLA analysis in coastal ocean 13
3.1. Comparison with the V14 CPP range estimates 15
3.1.1. Dependencies between parameters 15
3.1.1.1. Dependency on wave height 15
3.1.1.2. Dependency on radial velocity 16
3.1.1. SLA continuity over the Pacific box 17
3.2. Comparison of significant wave height estimates 18
3.2.1. Spectral analysis of the SWH 19
3.2.2. SWH Histogram 19
3.2.3. Dependencies between parameters 20
3.2.1. SWH cartography 21
3.1. Comparison with V14 CPP significant wave height estimates 22
3.1.1. Dependencies between parameters 22
3.1.2. SWH continuity over the Pacific box 23
3.2. Comparison of backscatter coefficient estimates 24
3.2.1. Spectral analysis of sigma0 24

3.2.2. **Sigma0 Histogram** **25**
3.2.3. **Dependencies between parameters** **25**
3.2.4. **Sigma0 cartography** **26**
3.2.5. **Sigma0 continuity over the Pacific box with the V14 CPP solution** **27**
3.1. Comparison of the mispointing angle estimates **28**
4. **Conclusion** **31**
5. **References** **32**

1. Introduction

1.1. Purpose and scope

This document aims at analysing the RDSAR (also known as Pseudo-LRM) method from TUDelft, in comparison with the one implemented within the CryoSat Processing Protoype (CPP) chain that was statistically validated on real data (then used for validating SAR-mode estimates over identical sea state).

A first attempt of assessment of the two RDSAR solutions was undertaken by comparing the Radar Altimeter Database System (RADS) retrievals from TUDelft with the CPP RDSAR level-2 outputs. Unfortunately the observed differences highlighted principally the well-known differences between MLE3 and MLE4 retrackers adopted by TUDelft and CPP respectively, instead of the more critical aspect in constructing RDSAR waveforms at the level-1 stage.

To overcome this problem, it has been decided to homogenize the level-2 processing by applying the same retracker (MLE4 from CPP) to the two sets of waveforms, and then to analyze their retrievals. Thus this approach permits to focus the interest on level-1 processing only.

A set of dedicated diagnoses has been used to evaluate the differences between both waveform generation methods, and see whether biases and noise performance computed for different estimated parameters (range, wave height, sigma0, and mispointing angle) are found to be consistent with those obtained from CPP or even better.

The description and the analysis of all the differences that are reported herein were discussed in a strong scientific collaboration with the algorithm expert/responsible who provides a very useful support to assess the performances of their algorithm, help to identify any unexpected behaviours and finally validate the content of this report.

1.2. Document structure

This document is structured into an introductory chapter followed by three chapters describing:

- the data used and coverage, and a short description of the two retracking algorithms to be compared (section 2),
- the analysis of the RDSAR L2 products through different diagnoses that are used to establish their performance (quantifying their skills and drawbacks) and their difference (section 3), and
- a discussion about these results (section 4).

2. Data and method overview

2.1. Data coverage and period

The TUDelft RDSAR solution was cross-compared with the validated v13 CPP RDSAR L2 products over large areas operated in SAR mode, between 60° north and 50° south in latitude, for the following two periods: July 2012 and January 2013, as shown in Figure 1. In the selected band of latitudes, SAR-Mode zones of different sea states are observed:

- The equatorial Pacific area was selected by ESA among those proposed by an expert validation group, considering that the zone met the following criteria required: low ocean variability (to ease the inter-mission calibration with conventional altimetry satellites like Jason 2), few occurrences of rain and sigma-0 blooms events (which could have different impacts on SAR and RDSAR), mean SWH around 2 meters and mean wind around 7 ms^{-1} (so the sea state is close to the mean conditions). This area was activated in SAR-mode since 7 May 2012 and reduced since 1 October 2012.
  This site has been used for successfully validating the CPP RDSAR data by cross calibrating with Jason-2 mission and analyzing the continuity between CPP LRM and RDSAR profiles at the LRM/SARM transitions [Moreau, 2013], [Labroue, 2014].
- The North East Atlantic area is an additional pool of useful data with varying sea state conditions wrt seasonal variation (very low wave heights with bloom events in July and high wave-heights in winter time), providing a much wider range of ocean wave heights for undertaking this study.
- The Agulhas current is a zone of interest where high waves are observed.
- The Mediterranean is a well-known region with calm seas (bloom events) also comprising large coastal areas dedicated to the evaluation of specific retrackers.

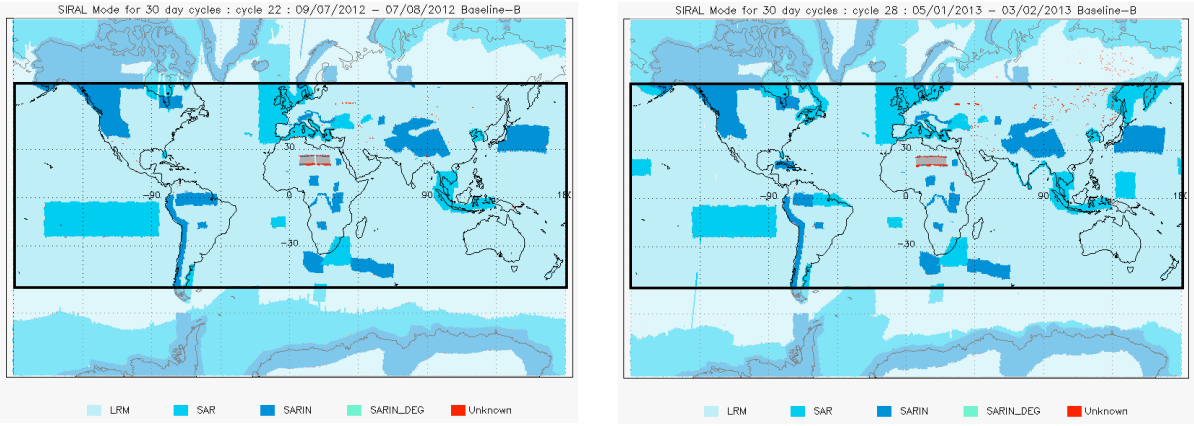

Figure 1: The mode mask, uploaded to CryoSat-2 in July 2012 (left panel) and January 2013 (right panel) (from

http://cryosat.mssl.ucl.ac.uk/qa/mode.php) with the selected box areas.

The 20-Hz geophysical parameters (range, significant wave height, and sigma-0) retracked by the TUDelft RDSAR solution are obtained from the CPP multilooked echo power. These estimated parameters are thus generated at the same time and along-track location as the ones processed by the SAR CPP numerical retracker, allowing both retrievals to be directly subtracted without the need to apply any geophysical model (e.g., wet and dry troposphere correction, ionosphere correction, tidal correction, dynamic atmospheric correction) or orbit elements (like the orbital ephemerides to derive a precise altitude) that may contribute to differences and lead to unclear conclusions regarding the comparison between the different processing approaches. This is especially true for the sea level anomaly (SLA) and other altimeter derived products like the wind measurements that account for corrections and/or models.

2.2. Method description

2.2.1. RADS RDSAR solution (TUDelft)

This method is fully described in [Scharroo, 2014].

2.2.2. CPP RDSAR solution

The method for the CPP RDSAR retracking is described in [Boy and Moreau, 2013] and validation results were already delivered in [Moreau, 2013], [Labroue, 2014].

2.2.3. Discrepancies

The major differences between the two RDSAR processing methods that are compared in this study are listed below:

- The RADS waveforms are oversampled by a factor of two (by zero-padding the complex echoes) producing power echoes of 256 bins. The CPP waveforms contain 128 samples.
- R. Scharroo reported at the CryoSat Workshop in Dresden [Scharroo et al., 2013] that the waveforms were shifted one gate too far to the left by error whereas the LPF filter was in the right place, meaning that the waveforms should be properly centered on gate 34 instead of gate 33 (counting from 0). This correction has been applied to the RDSAR waveforms in RADS before the introduction of the Jensen's oversampling. A 1-gate shift to the right has also been lately applied to the waveforms of the v14 CPP, but has not been taken into account in the v13 CPP which was originally adopted to serve in the framework of CP4O project for providing reliable reference data to compare new methods with. A very recent study has been conducted by CLS to precisely evaluate the difference between ocean parameters obtained through the two different versions of CPP (v13 and v14). These differences

are deemed important enough to be considered in the overall assessment results of the RDSAR TUDelft solution in comparison with the CPP one.

- The CAL2 (LPF) is already applied to the RADS and CPP waveforms. In RADS the LPF shape for the intermediate waveform samples is determined by linear interpolation between the 128 LPF values. The LPF shape is correctly aligned and does not need to be shifted to the right.
- In RADS, the pulse-to-pulse amplitude and phase corrections (from the IPF database) are applied to the echoes. This does affect the eventual shape of the PLRM waveforms. This is not done in CPP.
- Each echo is shifted in frequency to account for the radial velocity. This is accomplished by a phase shift that depends on the pulse index ("slow time") and the sample index ("fast time"). This will align the echoes around the tracking point after FFT. The Doppler shift (in frequency) effect is taken into account within the RADS waveforms. This is done to shift the nadir beam to be in the middle after a 2-D FFT. In other words, the parabola of peak power obtained after the 2-D FFT will have its top located around the tracking gate (horizontally) and at the centre of the "slow time" coordinate (vertically). Currently, this is not considered in the CPP processing. However, this will not have any consequence on the resulting waveform: after a 2-D FFT it only constitutes a vertical shift that disappears in the averaging (next step), while the horizontal position remains unchanged.
- The AGC is applied on CPP waveforms whereas it is not applied on RADS side. In RADS it is accounted for in the waveform scale factor.
- Both processing approaches have identified the presence of a time calibration bias which produced altimeter measurement errors that depend on the altitude rate. For RADS, different timing biases are applied for different data. These timing biases are included in the time field on the RADS data and are accounted in the orbital altitude. For CPP (v13), a constant timing bias of +176 microseconds is determined and accounted in the precise orbit.
- Also notice that the tracker range from RADS is counted from gate 34 in the 0 to 127 scale of the window delay, whereas it is starting from gate 0 in the CPP products, leading to an extend of 34*c/2B ~ 15.92m in the RADS tracker range values to subtract before range computation.

2.2.4. **Edited data**

Data editing is necessary to remove altimeter measurements having lower accuracy. To analyze the consistency between both RDSAR solutions in open ocean, only valid ocean data are selected (removing data corrupted by sea ice and rain). Specific editing criteria are applied, based on thresholds on different parameters.

3. Validation results and overall assessment

The overall objective of this validation exercise is to assess the performance of the innovative TUDelft RDSAR waveform creation solution, highlighting the main features, discrepancies, advantages and drawbacks of this method while comparing to the CPP SAR products (V13 and V14).

The assessment task is conducted with robust and standard methods that are classically used in current Cal/Val analyses, to precisely validate and cross-calibrate different algorithms.

For this purpose, the validation of the TUDelft RDSAR solution is performed through the following set of diagnoses:

- Estimated parameters cartography to visualize their geographic locations and identify their dependencies on geophysical signals (SWH, calms or sigma-0 blooms or rain areas, but also vertical velocity);

- Diagnoses on the performances of the waveform fitting (plot of the misfit between the measured waveforms and the fitted model as a function of SWH);

- Plots of the parameters themselves (parameter profiles as a function of time, histograms, dispersions or scatter-plots);

- Spectral analysis of parameters (sea level anomalies, SWH or sigma-0);

- Analysis of the two data sets in the coastal domain.

These diagnoses are performed at higher data set rhythm, 20-Hz.

3.1. Performances of the waveform fitting

3.1.1. Misfit analysis

A first interesting diagnostic for this comparison consists in evaluating the mean quadratic error (MQE), which measures the misfit of the RDSAR models to the echo waveforms. This indicator allows the evaluation of the accuracy of the retracking algorithm to model real echoes, which can impact the quality of the estimates.

Figure 2 represents the mean MQE over the entire selected area in July 2012 (right panel) and January 2013 (right panel). These plots show a good agreement between both solutions, but with a noticeable lower mean misfit of the V13 CPP than the TUDelft solution one. Also note that the misfit cloud for CPP and TUDelft solution covers each other totally, exhibiting a very similar behaviour.

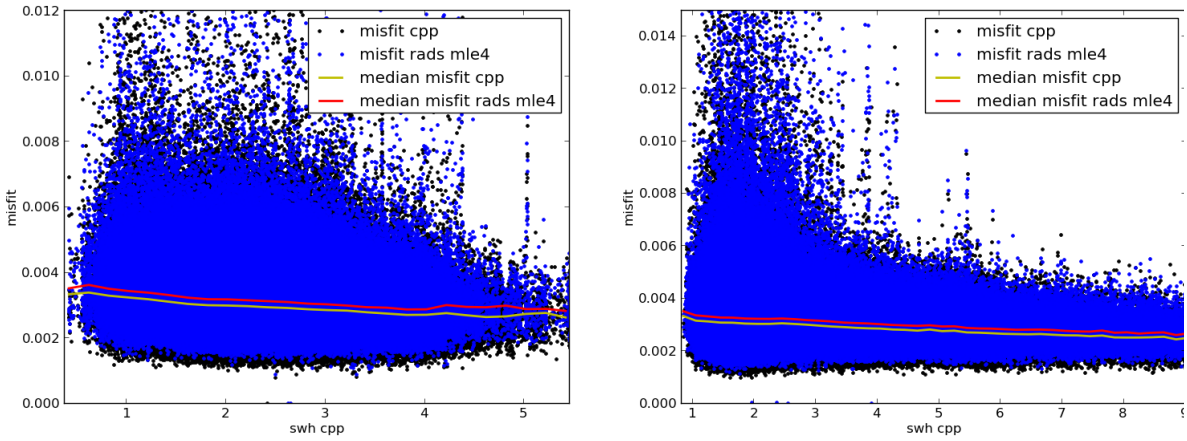

Figure 2: Mean misfit curve for v13 CPP (plotted in yellow) and TUDelft solution (plotted in red) as function of SWH in July 2012 (left panel) and January 2013 (right panel).

Figure 3 shows that the misfits are quite comparable over open ocean with differences not exceeding few 10-4 (<5%). Highest misfit differences are located in coastal area but still not significant.

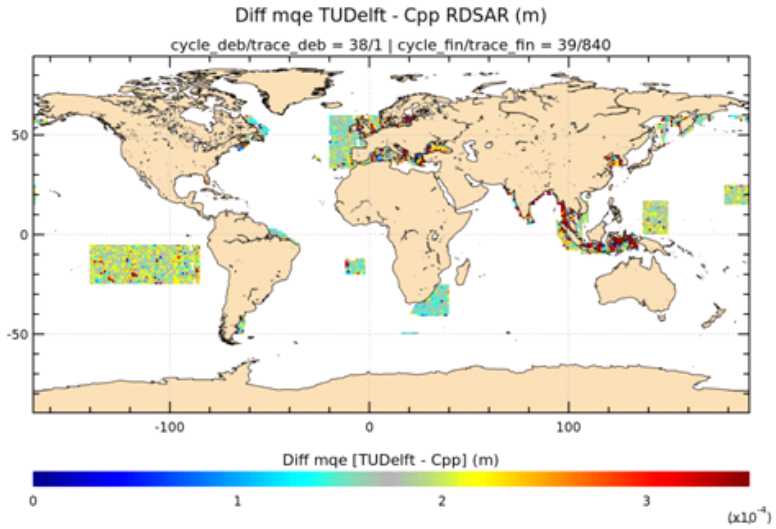

Figure 3: Map of misfit difference in January 2013 for ascending passes

3.2. Comparison of range estimates

This section presents the results of the CLS analysis bench obtained with the two methods (TUDelft RDSAR solution and CPP one), to quantify their performances. In the following subsection the range estimates have been compared through several metrics pointing out their similarities and discrepancies.

3.2.1. **Spectral analysis of the SLA**

The two spectra are obtained by integration of many elementary spectra computed on continuous data segments, for which an averaged SWH of 2.5m is observed.

From Figure 4, we can see that both solutions measure exactly the same content of the oceanic signal at high wavelengths (>100km), but exhibit some discrepancies at smaller wavelengths in particular for scales 10-80 km (the region of the spectral hump) where the energy of the SLA from the CPP solution appears slightly higher. Also, one can notice that the 20 Hz (the full altimetry resolution) -noise level of the TUDelft is a little bit lower than the CPP one (10.6 cm against 11.2 cm).

Both RDSAR solutions are however affected by correlated errors that are seen as a spectral hump.

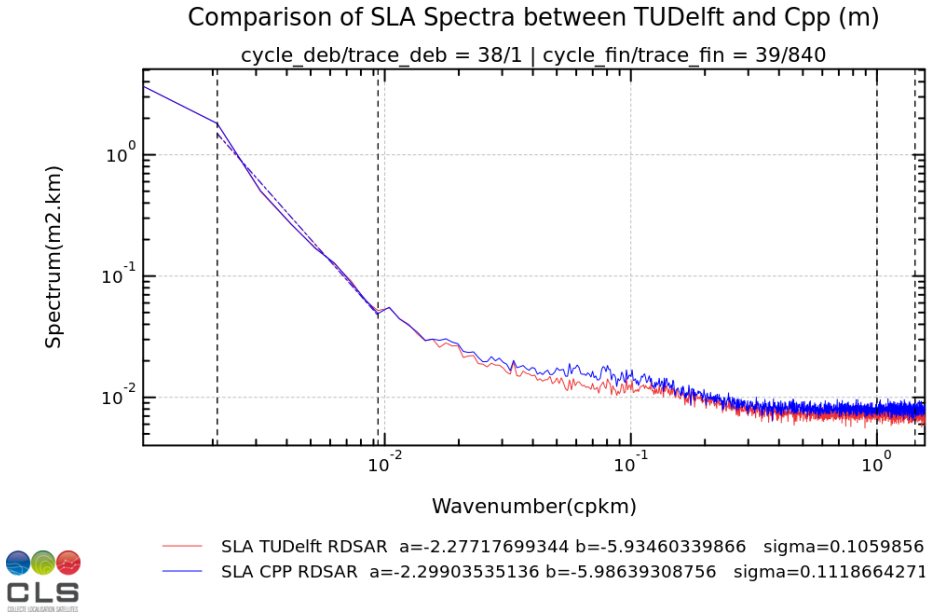

Figure 4: Mean SLA spectrum for v13 CPP (plotted in blue) and TUDelft solution (plotted in red) in January 2013 over the entire SAR-mode area. The abscissa represents the wavelengths (on the top of the plot) or equivalently the wavenumbers (1/km).

The Figure 5 shows the agreement between the SLA from RADS product retracked by MLE4 and the SLA from the CPP product (v13) along a pass in the Pacific. Differences at centimeter are observed in this example.

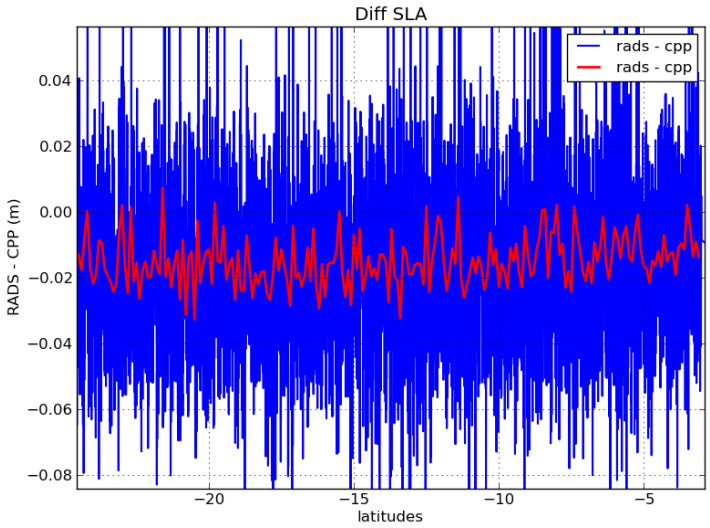

Figure 5: Differences of SLA from TUDelft RDSAR solution and V13 CPP dataset as function of the latitude for one pass located in the Pacific box. Differences plotted at 20-Hz in blue and averaged differences per band of latitudes in red.

Notice that, in the SLA computation, the range and orbit field differ between the two products. On the other hand, the same geophysical corrections are applied. The range measurement is determined by adding the estimated epoch of the leading edge of the waveform (the tracking point epoch) to the tracker range. The orbit is usually corrected from time tag bias. However different processing may be applied to calculate this correction.

Next figures show, in left panel, the differences of tracker range, and, in right panel, the differences of estimated epoch (both derived from the MLE4 ocean retracker). On these plots a non-negligible trend between tracker range values and a mean bias of 67 cm is shown. There is also a trend in estimated epoch but in opposite direction (one gate shift is applied to CPP tracking point epoch to ease the comparison). These differences may be explained by a difference in how the 20-Hz waveform power is generated (difference in processing, notably the time tag computation for the 20-Hz measurement, and the echoes alignment). This figure also shows differences of orbit values that are likely related to differences in time tag bias correction processing.

Note that the SLA differences shown in Figure 5 are obtained after removing a systematic bias of 70cm between both tracker ranges and correcting the V13 CPP estimated epoch of one gate.

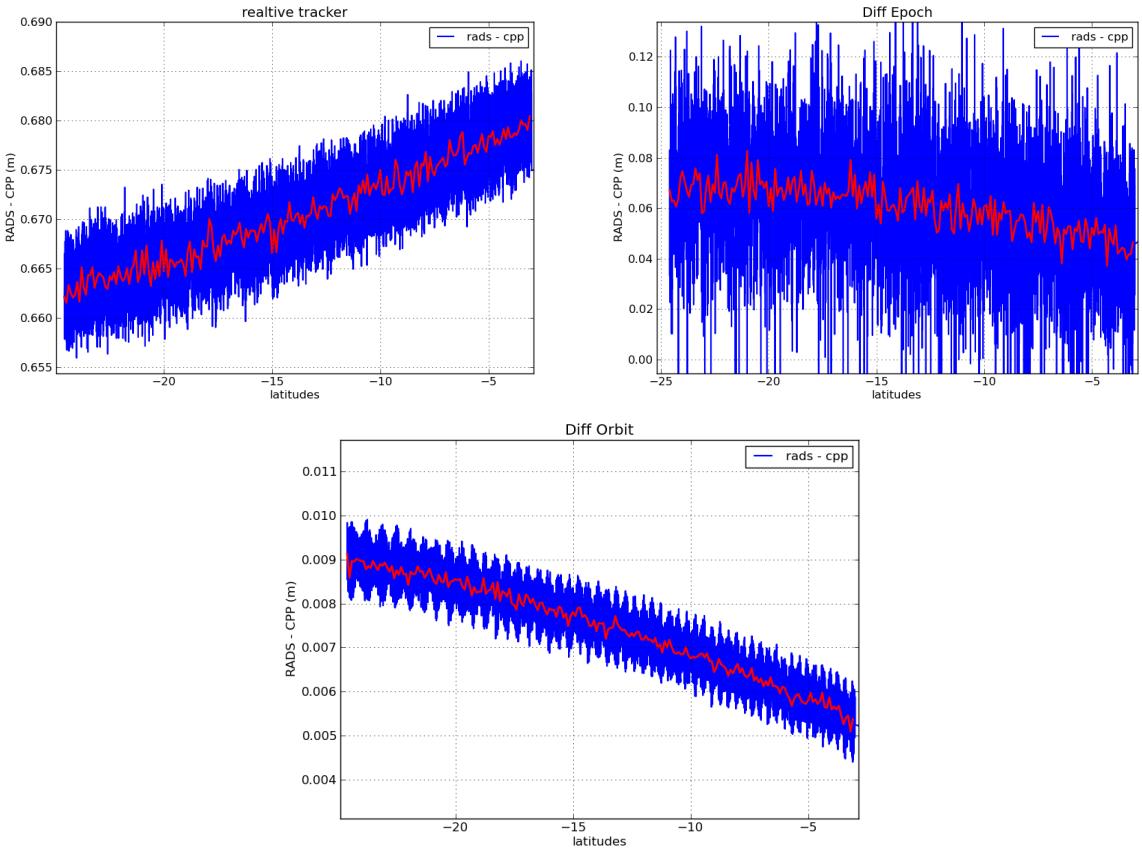

Figure 6: Differences of 20-Hz (in blue) tracker range (upper left panel), estimated epoch (upper right panel) and orbit corrected from time tag bias (bottom panel) from TUDelft RDSAR solution and V13 CPP dataset as function of latitude for one pass located in the Pacific box, and averaged differences per band of latitudes (in red).

3.2.2. SLA Histogram

The comparison between the TUDelft RADS solution and V13 CPP products underlines a quite low global bias of near 2.1 cm in range (LUT are applied on RADS range).

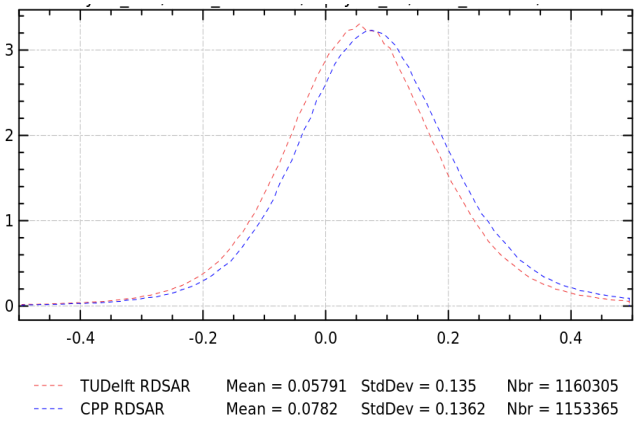

Figure 7: Histogram of 20-Hz SLA for the ESRIN SAR solution (in red) and V13 CPP (in blue) in January 2013 (ascending passes).

3.2.3. **Dependencies between parameters**

3.2.3.1. Dependency on wave height

The results are presented separating ascending and descending passes since the radial velocity comes up with different values at the same location that may impact the estimates.

To assess the consistency between 20-Hz SLA calculated for both solutions, their difference (or residual) has been computed as function of the filtered SWH, for ascending and descending passes, over two months (July 2012 and January 2013). The following figures (left panel of the Figure 8) show that the 20 Hz SLA residual is of several centimetres and depends on wave height. A similar dependency is observed for ascending and descending passes (around 0.5% SWH), with however a constant bias. We can also notice that the discrepancy between ascending and descending passes in the Pacific box is more significant for the RADS solution (see in Figure 9) and in this case, thus less consistent.

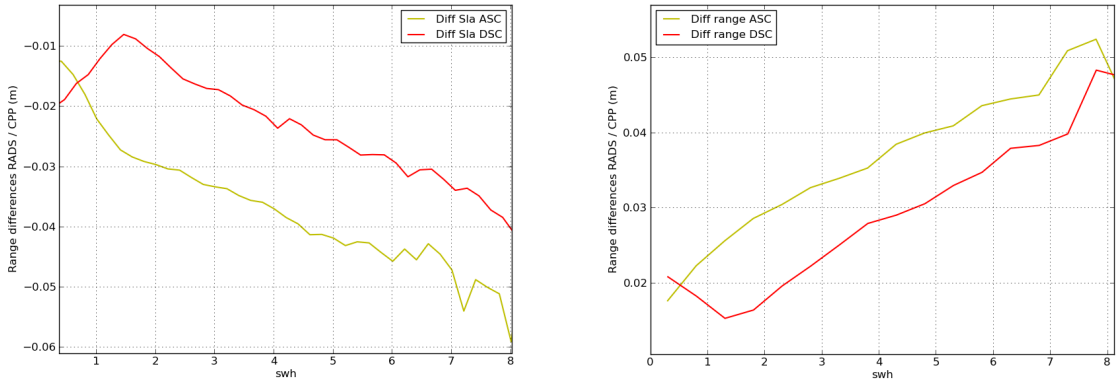

Figure 8: Differences of SLA (left panel) and range altimeter (right panel) from TUDelft solution and V13 CPP dataset as function of filtered SWH over two months (July 2012 and January 2013).

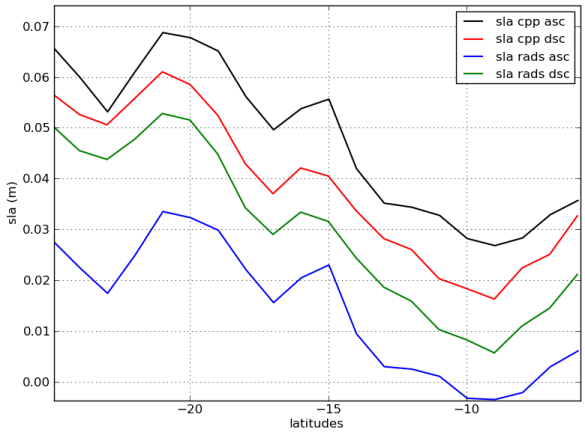

Figure 9: SLA computed on ascending and descending passes in the Pacific box for both solutions as function of band of latitudes

3.2.3.2. Dependency on radial velocity

The following diagnostics aim at identifying possible dependencies of the difference of 20-Hz ranges on the radial velocity. In Figure 10, the residual is plotted versus SWH and the radial velocity for July 2012. Those results show apparent dependencies of the residual measurements with respect to wave heights and to the radial velocity. If the dependency on wave height may be explained by the one-gate shifted waveform error in the v13 CPP product, the dependency on radial velocity is due to a difference in how to generate the 20-Hz averaged echo within the processing. The analysis of sea surface height discrepancies at ground track intersections (crossovers) with larger amount of data (over a longer time period and in global) would permit to assess which one of the two methods better correct of the time tag bias.

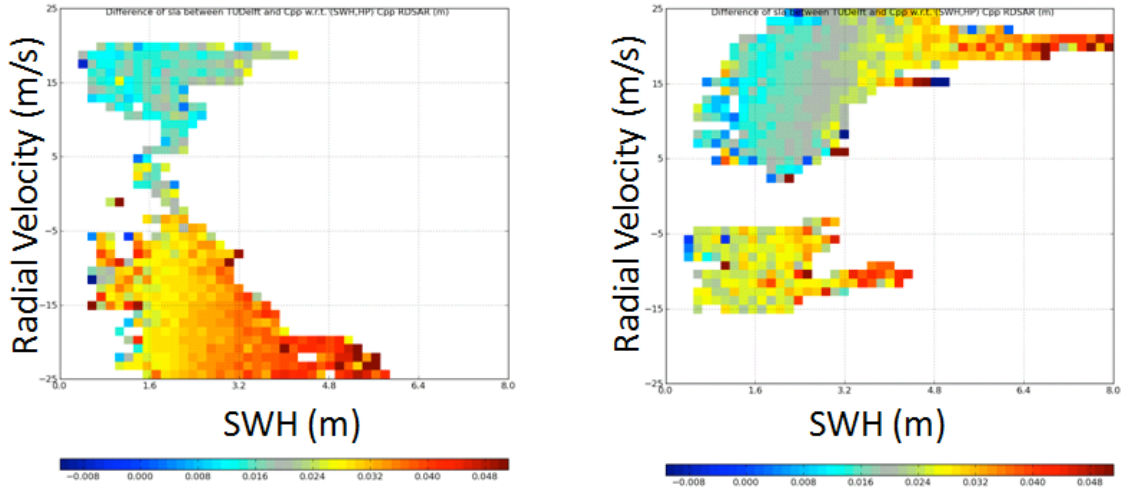

Figure 10: Dependencies of 20-Hz range residual with filtered SWH and radial velocity for ascending (left panel) and descending passes (right panel) in July 2012.

In Figure 11 orbit differences are plotted as function of the radial velocity. Though orbits are corrected from time tag bias, it remains a dependency on radial velocity. This result underlines a residual time tag bias around 380 us.

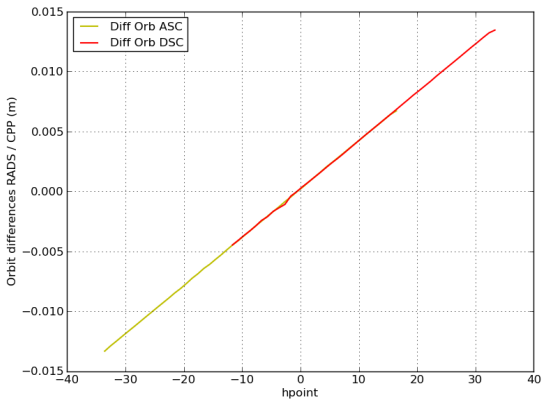

Figure 11: 20-Hz corrected orbit residual in function of radial velocity for ascending and descending passes in July 2012.

The Figure 12 and Figure 13 show the 20-Hz SLA residual as function of the latitude and of the radial velocity respectively, in the Pacific and N-E Atlantic SAR-mode areas. Those results are consistent with the previous plots and confirm the strong dependency of the residual to the radial velocity (often been referred to as the butterfly diagram). From the plot in Figure 13, we can estimate a time tag bias of 541 us between RADS and V13 CPP SLA. A part of this bias (380 us) is due to the observed differences in orbits (Figure 11).

In Figure 12, the impact of the residual time tag bias on the SLA difference is clearly seen, which then leads to discrepancies at the same location between ascending and descending passes.

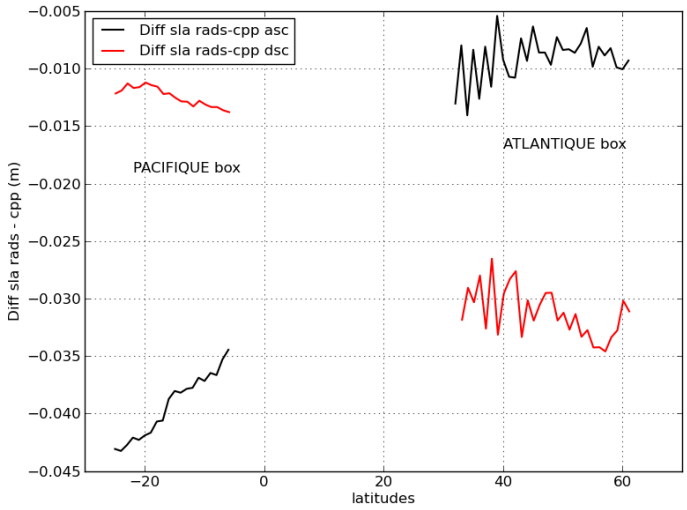

Figure 12: Differences of SLA from TUDelft solution and V13 CPP dataset as function of the latitude for ascending (black curve) and descending (red curve) passes in the Pacific and North East Atlantic boxes in July 2012.

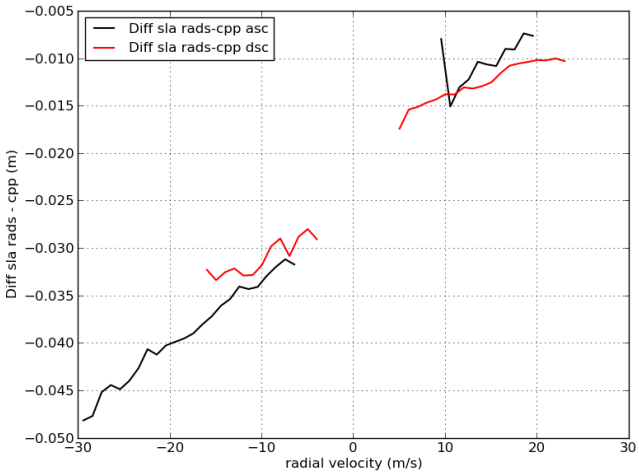

Figure 13: Differences of SLA from TUDelft solution and V13 CPP dataset as function of the radial velocity for ascending (black curve) and descending (red curve) passes in the Pacific and North East Atlantic boxes in July 2012.

3.2.4. SLA cartography

A mean map (averaged values in each 2°x2° grid bins) of the 20-Hz SLA residual between TUDelft and V13 CPP RDSAR solutions is plotted in Figure 14 for ascending and descending passes in July 2012.

In first, we can observe that the geographical distribution of the mean residual is different between ascending and descending passes, as already shown in Figure 8. Also note the presence of strong North-South biases, showing a clear correlation of the SLA difference with the radial velocity variations.

There are missing track portions in the RADS data. Whilst no impacts on this assessment would be expected, this absence of a small number of data products in the RADS data set should be investigated.

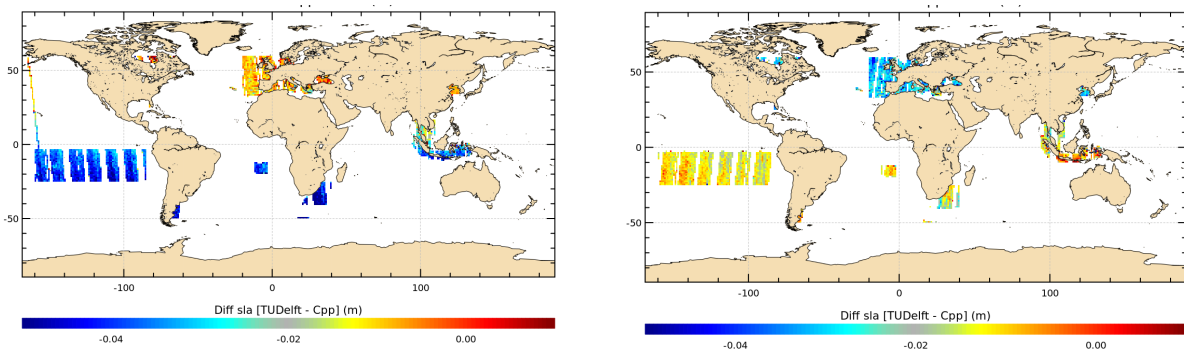

Figure 14: Difference of SLA from TUDelft RDSAR solution and V13 CPP for ascending (left panel) and descending passes (right panel) in July 2012.

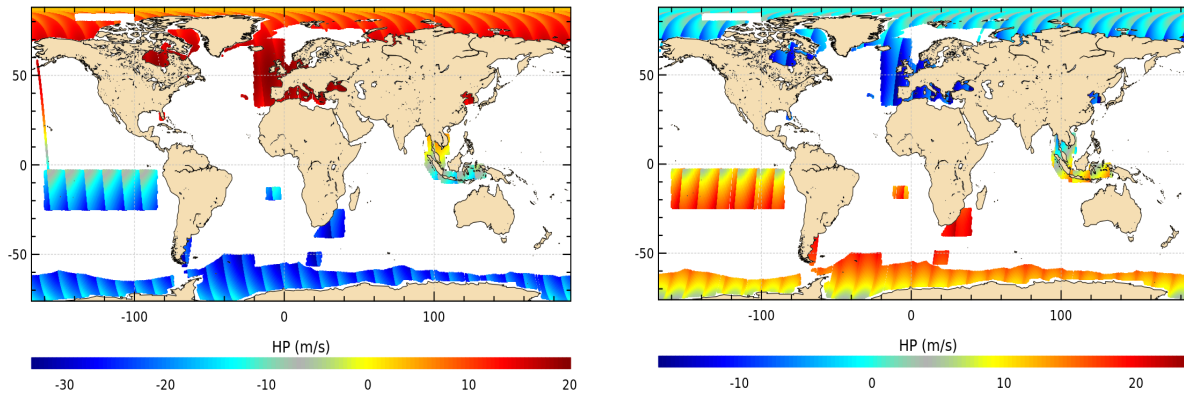

Figure 15: Map of the radial velocity values for ascending passes (left panel) and descending passes (right panel) in July 2012

3.2.5. SLA analysis in coastal ocean

It is also important to evaluate the ability of the two different processing schemes to work near the coasts. We can see on Figure 16 quite similar behaviour with few non valid RADS and CPP estimates while approaching the coast.

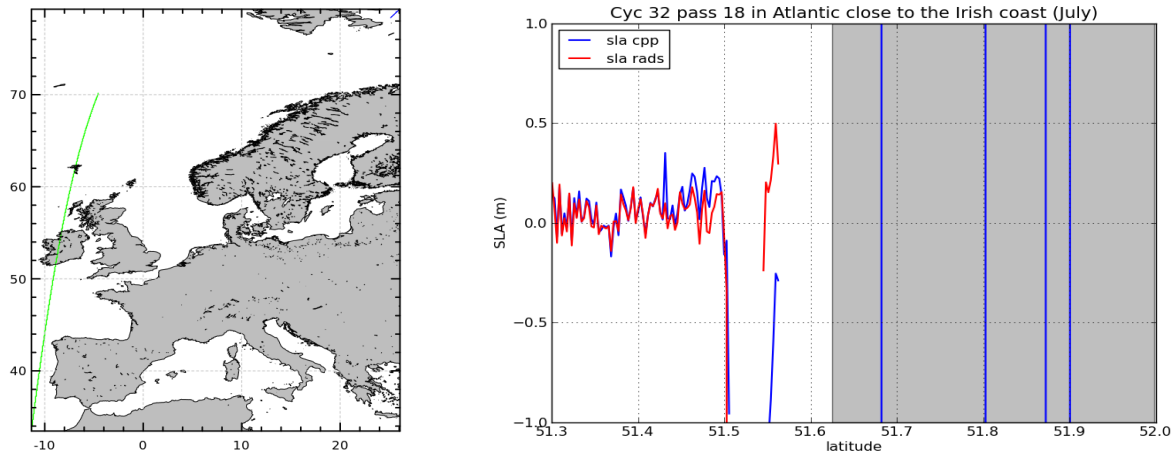

Figure 16: TUDelft RDSAR solution (in red) and V13 CPP (in blue) SLA profiles in July 2012 over the North East Atlantic area. Shaded region corresponds to land.

This analysis is performed statistically over a large number of observations to assess the consistency of the two processing schemes in the coastal region.

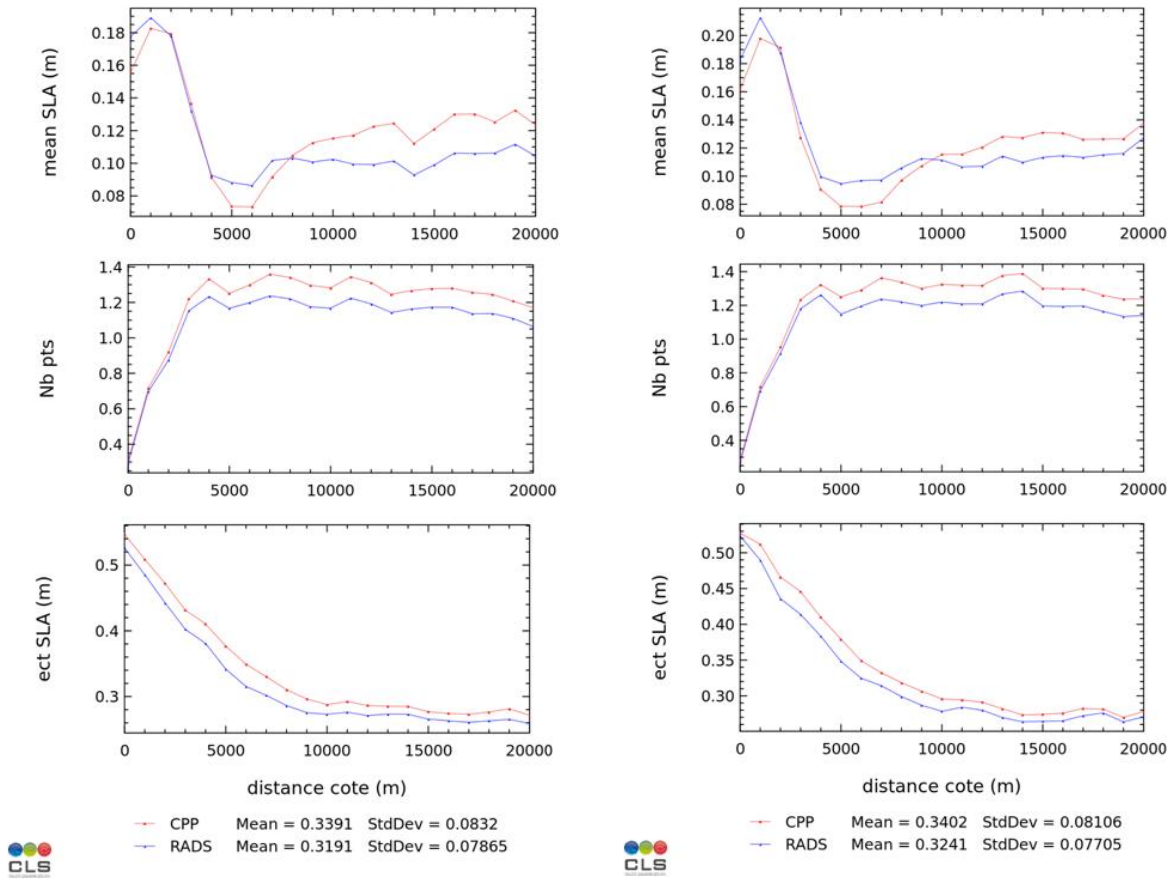

Figure 17: SLA statistics (mean, number of points, standard deviation) as function of the distance to the coast by using the TUDelft RDSAR solution (in blue) and V13 CPP (in red) retrackers in ascending (left panel) and descending (right panel) passes.

Figure 17 shows the mean SLA between 0 and 20km from shoreline and the associated standard deviation. From this figure, no clear strong differences between estimates are apparent, except a slight increase of the standard deviation of valid measurements near the coast with the CPP solution. In the other hand, one can notice that the number of valid measurements from CPP processing is slightly higher in deep ocean.

3.1. Comparison with the V14 CPP range estimates

The new v14 CPP product that is corrected from the one-gate shifted waveform error is compared in first to the previous version (v13) product then to the TUDelft RDSAR solution.

3.1.1. **Dependencies between parameters**

3.1.1.1. Dependency on wave height

The Figure 18 shows the impact of the correction of the one-gate shifted waveform error on the range. From this plot, we can notice that the range difference depends on wave height in the same way as it is observed while comparing ranges between the TUDelft solution and the v13 CPP one (shown in right panel of the Figure 8). **Thus this correction mitigates the discrepancies between TUDelft and CPP RDSAR solutions.**

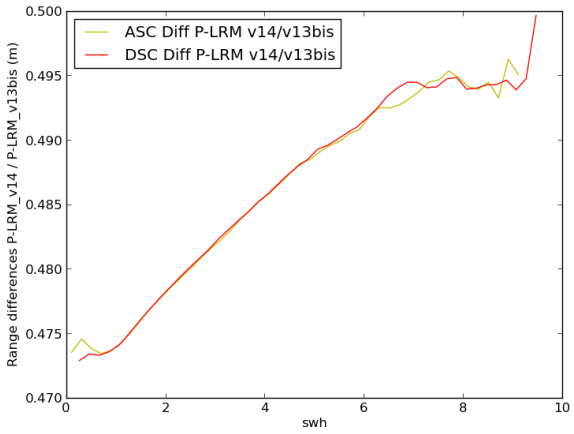

Figure 18: Difference of range between the two different versions of CPP: before (v13) and after (v14) correcting the one-gate shifted waveform error.

Analysis of the differences between the TUDelft solution and the v14 CPP one (see panel right of Figure 19) confirm the previous analyses. From this plot we can clearly see that the dependency on wave height is greatly reduced (in comparison with Figure 8). However a (quite low) dependency remains for the ascending satellite passes, that is found to be related to some inconsistency observed with the ascending SLA from TUDelft solution (as shown in the blue curve in Figure 19). These plots also permit to assess the remaining residuals (that may be due to other parameter dependency) that will be discussed in the following section.

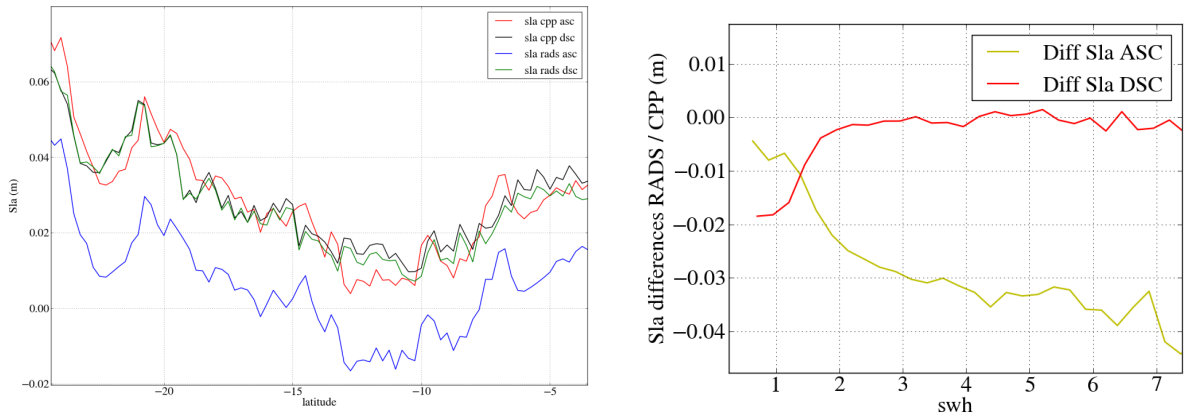

Figure 19: SLA plot of TUDelft solution and V14 CPP dataset (right panel) as function of filtered SWH, and their differences (left panel) as function of band of latitudes over two months.

3.1.1.2. Dependency on radial velocity

The estimated time tag bias of 541 us has been taken out in the difference of SLA between the TUDelft solution and the V14 CPP one, and the corrected differences are then plotted in Figure 20. Once the SLA differences are corrected for the timing bias, the curves appear quite constant (only few millimetres of discrepancy reported from low to high wave height) and similar for ascending and descending passes (in comparison with the panel right of Figure 19). In particular this correction is found to compensate the TUDelft SLA residual between ascending and descending passes as shown in Figure 21 before and after correction.

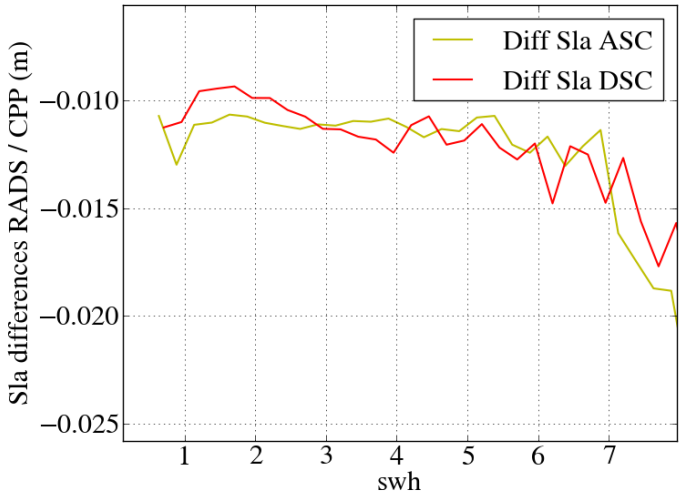

Figure 20: Corrected differences of SLA from TUDelft solution and V14 CPP dataset as function of filtered SWH over two months (July 2012 and January 2013).

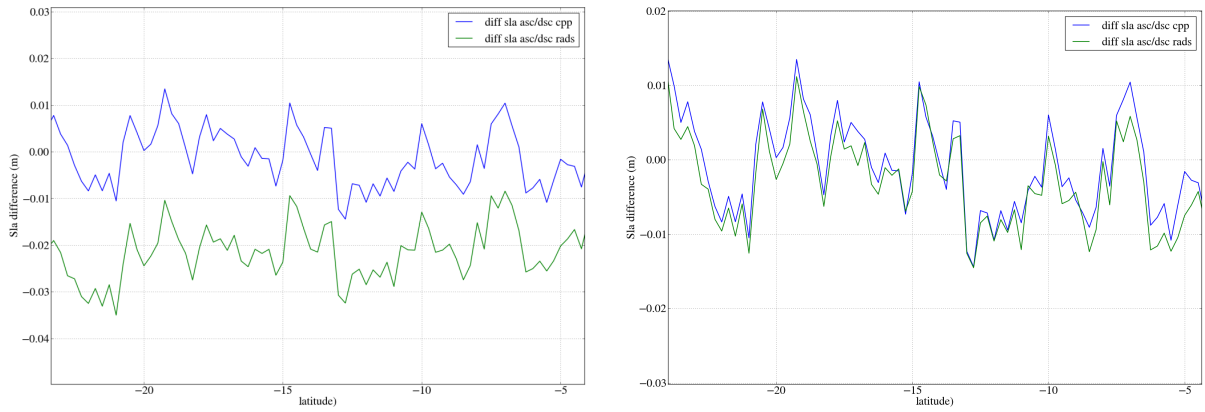

Figure 21: Mean differences of SLA (left) between ascending and descending passes as function of band of latitudes for the TUDelft solution (in green) and the V14 CPP dataset (in blue) over two months (July 2012 and January 2013). Mean differences of SLA after timing bias correction of -541us applied on TUDelft data sets (right)

3.1.1. SLA continuity over the Pacific box

The analysis is done over the patch of the Equatorial Pacific over July 2012 and January 2013, separating between ascending and descending satellite passes.

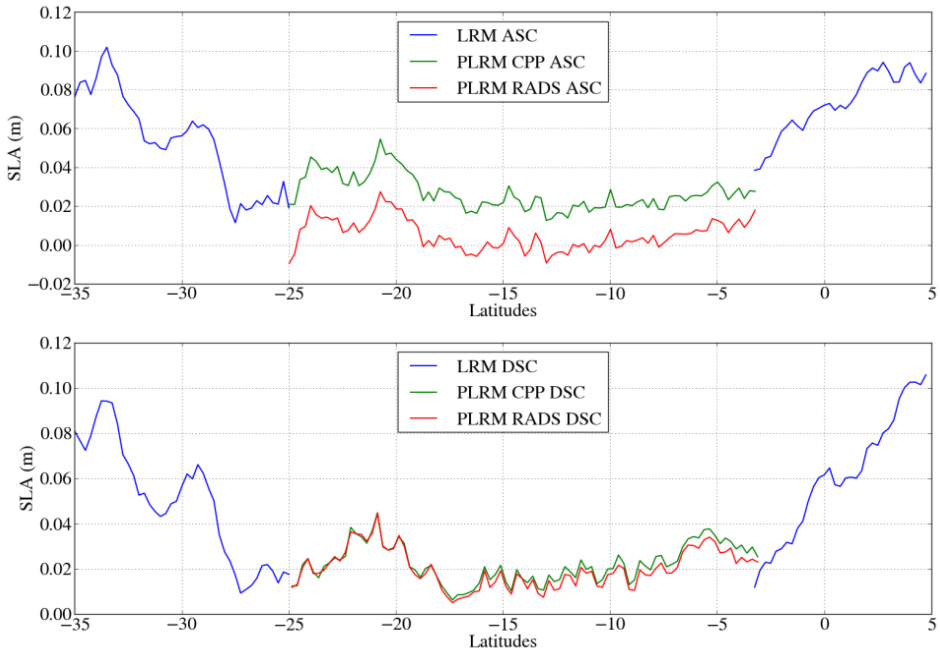

Figure 22: Mean SLA as function of band of latitudes for the TUDelft solution (in red), the V14 CPP dataset (in green) and the CPP LRM (in blue) over two months (July 2012 and January 2013).

The Figure 22 shows the SLA from TUDelft and V14 CPP RDSAR solutions, averaged per band of latitudes over the Pacific SARM area. It also represents the mean of the CPP LRM SLA obtained on the same period but outside of this region. From this plot, we can observe a seamless transition between LRM and RDSAR processing at -25° and -3°. Indeed the agreement is remarkable between LRM and V14 CPP RDSAR SLA profiles, with a bias below the centimetre level. Similarly the descending tracks exhibit no discontinuity between LRM and TUDelft profiles. However the ascending tracks do not match as well (a bias seems to be close to 2.5 cm) but could be easily corrected by applying the dedicated timing bias correction as computed previously.

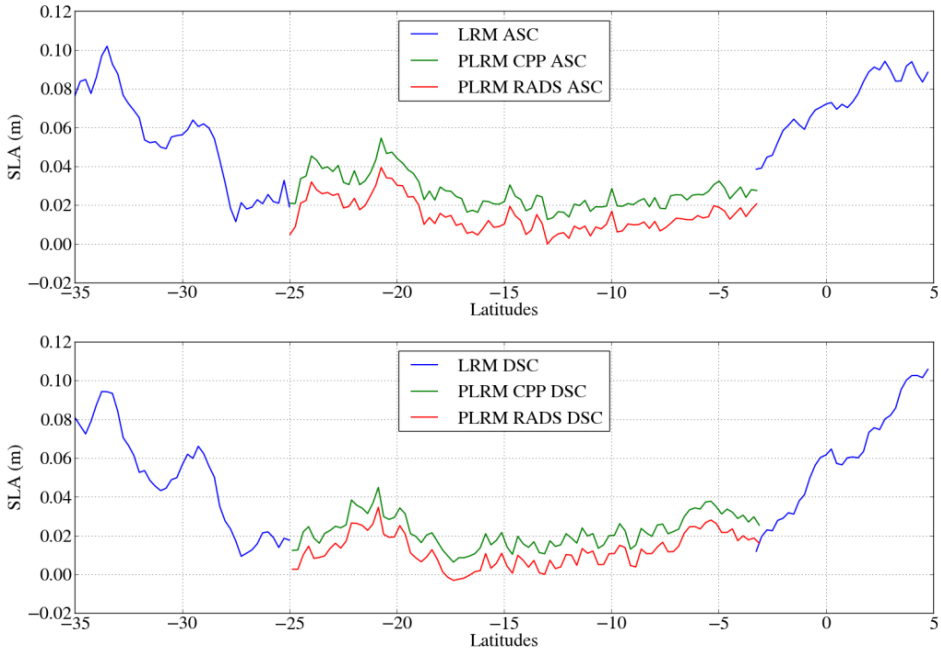

Figure 23: Mean SLA as function of band of latitudes for the TUDelft solution corrected of -541us timing bias (in red), the V14 CPP dataset (in green) and the CPP LRM (in blue) over two months (July 2012 and January 2013).

The Figure 23 shows the SLA from both solutions, after applying timing bias correction of -541us on TUDelft data sets. We can see afterwards a better consistency between TUDelft SLA from ascending and descending tracks. A remaining system bias may have to be found to ensure that CPP v14 and RADS PLRM data are fully in line.

Also note that given the oceanic variability at both transitions, it is remarkable to find such an agreement between LRM and RDSAR observations.

3.2. Comparison of significant wave height estimates

The same analysis is done on significant wave height (SWH). A comparison between the TUDelft solution and the V13 CPP one is performed first.

3.2.1. Spectral analysis of the SWH

On the Figure 24, one can see that the two spectra are well overlapped with each other. We also notice that the SWH noise level is around 65cm at 20 Hz for both processing (3cm lower for the TUDelft solution at 2m SWH, probably due to the employed zero-padding method that is found to reduce noticeably the variance in estimated SWH. However the observed reduction in SWH variance is lower than expected by a factor of 2).

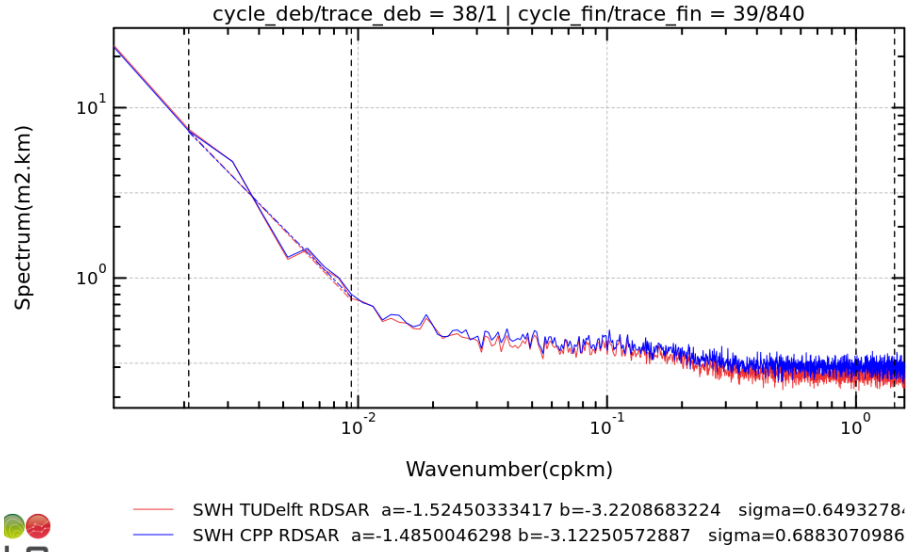

Figure 24: Mean SWH spectrum for V13 CPP (plotted in blue) and TUDelft solution (plotted in red) in January 2013 over the entire SAR-mode area. The abscissa represents the wavelengths (on the top of the plot) or equivalently the wavenumbers (1/km).

3.2.2. SWH Histogram

Figure 25 shows the SWH histograms for the two RDSAR solutions. One can observe very similar histograms with only few cm (< 3cm) of difference.

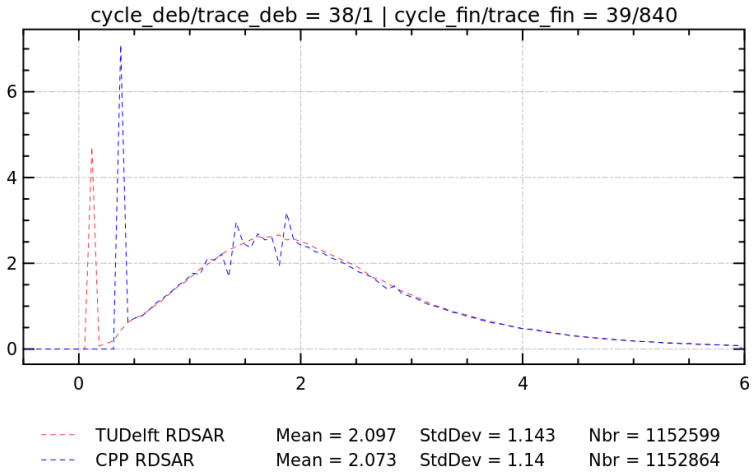

Figure 25: Histogram of 20-Hz SWH from TUDelft RDSAR solution (in red) and V13 CPP (in red) in July 2012.

3.2.3. Dependencies between parameters

We now analyse the sensitivity of the SWH residual to the radial velocity and wave heights.

The Figure 26 shows the 20-Hz SWH residual in function of filtered wave heights for the two selected periods. From this figure, we can notice that the residual depends noticeably on wave height. Higher differences are observed at very low wave height (up to -15cm). Then the plot tends to a mean bias of 5cm.

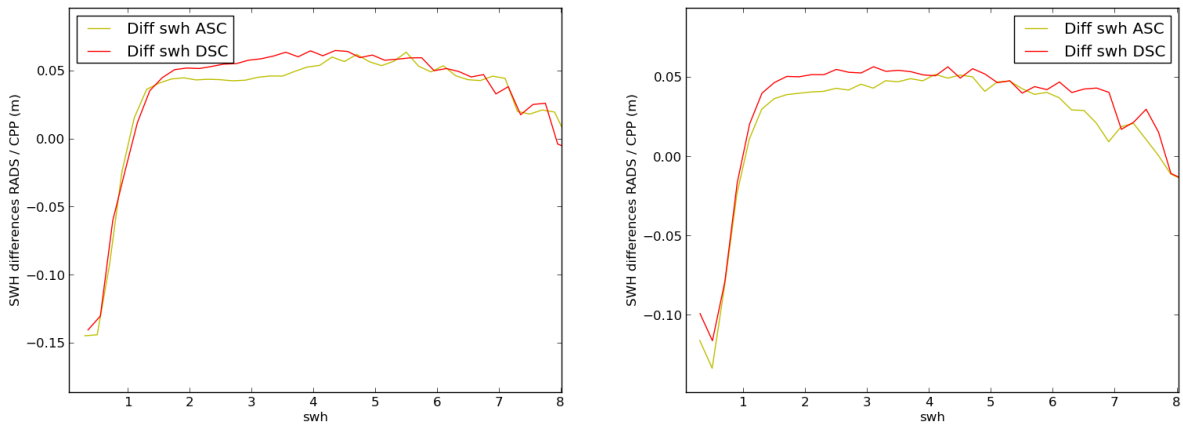

Figure 26: Dependencies of 20-Hz SWH residual with filtered SWH, in July 2012 (left panel) and January 2013 (right panel).

In Figure 27 the 20-Hz SWH residual is plotted versus SWH and the radial velocity for ascending (left panel) and descending passes (right panel) in January 2013. From these figures, one can observe that the 20-Hz SWH residual measurements have no apparent dependency on the radial velocity (low enough to be neglected). The SWH difference appears to be however correlated to SWH particularly at very low wave height as already pinpointed. Elsewhere a bias of 5cm is observed.

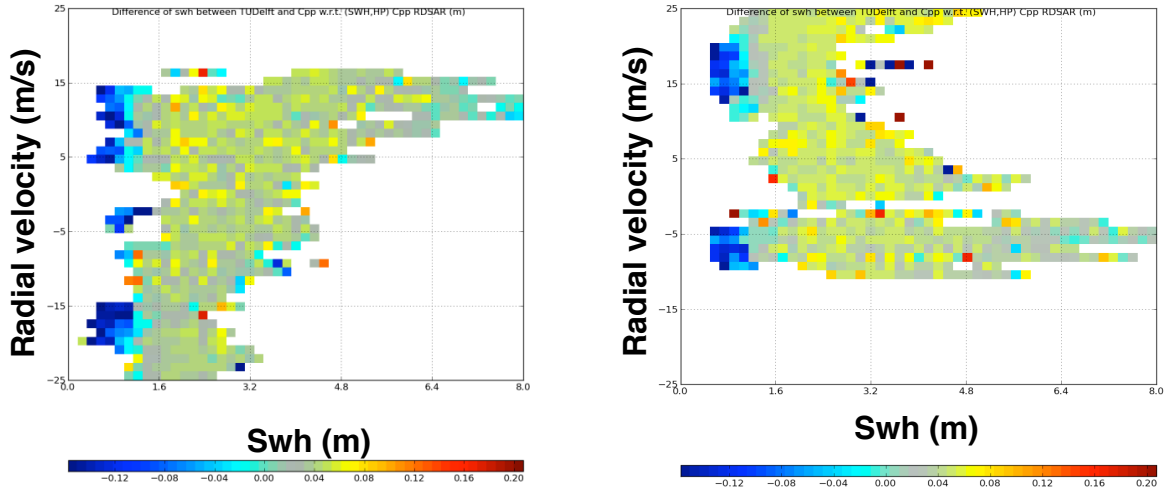

Figure 27: Dependencies of 20-Hz SWH residual with filtered SWH and radial velocity in Jan 2013 for ascending (left panel) and descending (right panel) passes.

3.2.1. **SWH cartography**

A global map reveals that the SWH residual is clearly correlated to the wave height (Figure 28 and Figure 29), though the SWH difference is low (up to 5cm). Furthermore, no dependence between the SWH residual and other parameters (such as the radial velocity and mispointing angles) is found.

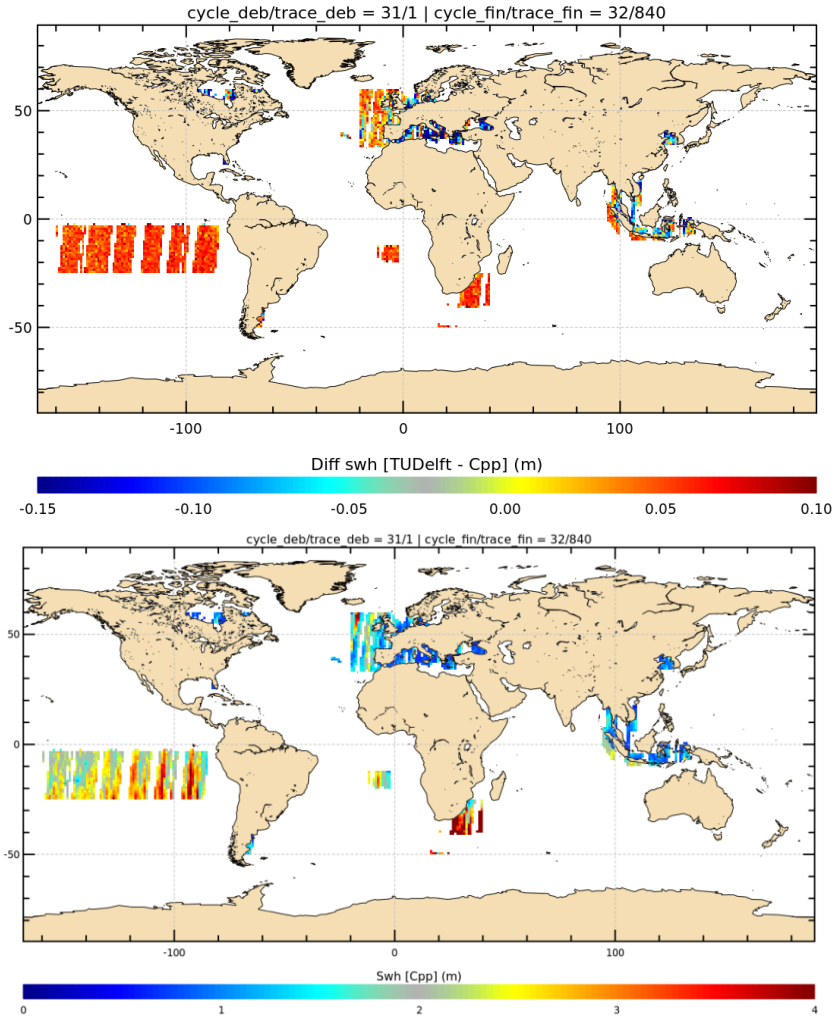

Figure 28: Difference of SWH between TUDelft and V13 CPP (top panel) and map of SWH in July 2012 (bottom panel) for descending passes.

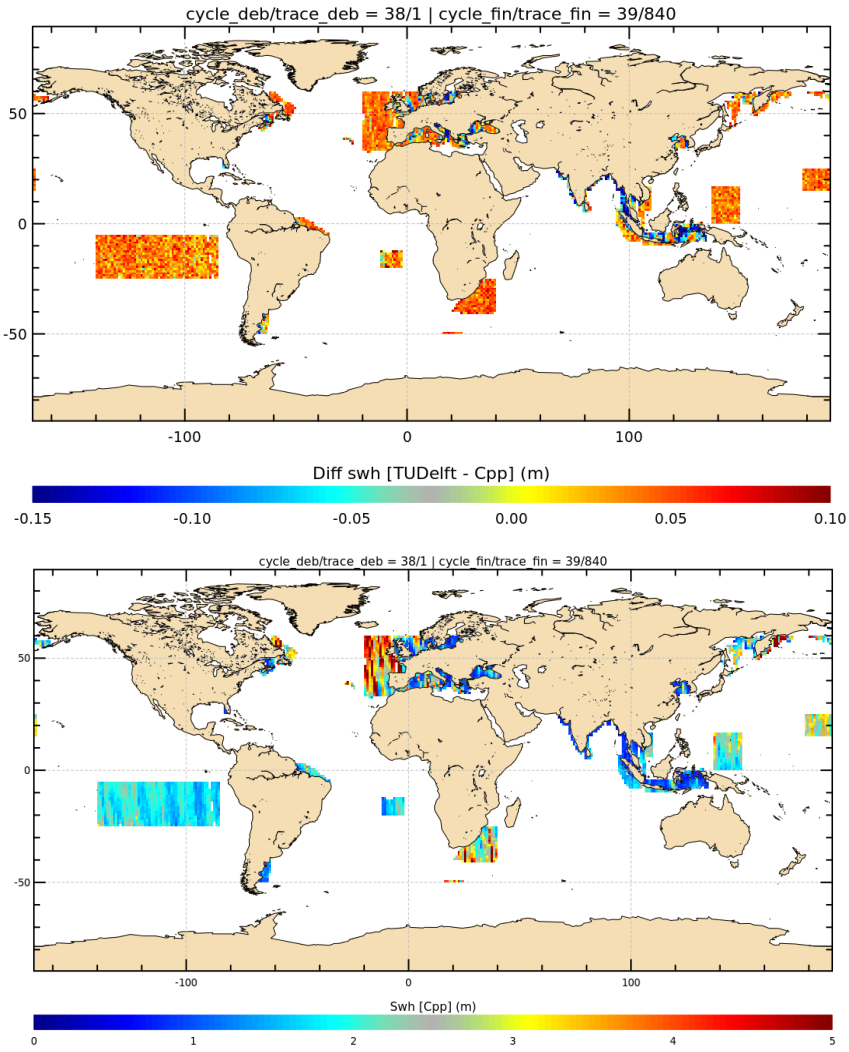

Figure 29: Difference of SWH between TUDelft and V13 CPP (top panel) and map of SWH in January 2013 (bottom panel) for ascending passes.

3.1. Comparison with V14 CPP significant wave height estimates

3.1.1. Dependencies between parameters

The SWH differences obtained from the two RDSAR solutions (see Figure 26) are found to have quite similar pattern compared with the plots of difference between 20-Hz SWH estimates from the two versions of CPP (see Figure 30). As expected we can see that the wave heights from the V14 CPP product better match those from the TUDelft RDSAR solution as shown in Figure 31. Only two centimetres of differences at maximum appear between both RDSAR solutions.

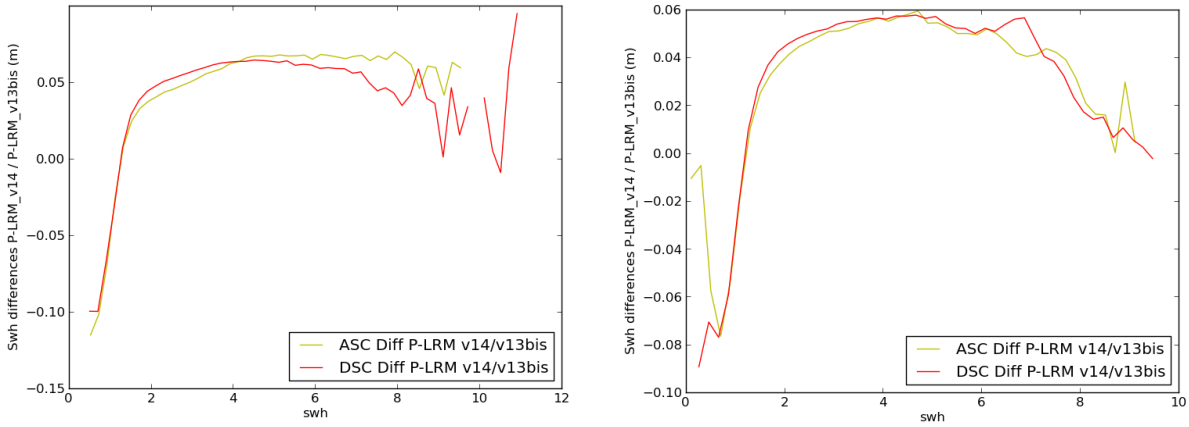

Figure 30: Dependencies of 20-Hz SWH residual with filtered SWH between V13 CPP and V14 CPP, in July 2012 (left) and January 2013 (right).

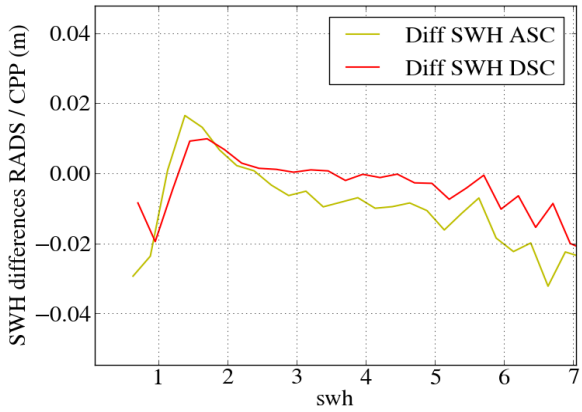

Figure 31: 20-Hz SWH residual between TUDelft and V14 CPP solutions as function of filtered SWH, for ascending and descending passes.

3.1.2. SWH continuity over the Pacific box

The analysis is done over the patch of the Equatorial Pacific over July 2012 and January 2013, separating between ascending and descending satellite passes.

As for the previous analysis of continuity (Figure 22), Figure 32 shows the SWH profiles. From this plot, we can observe very similar RDSAR (TUDelft and V14 CPP) SWH curves and a seamless transition between LRM and RDSAR processing at both transitions.

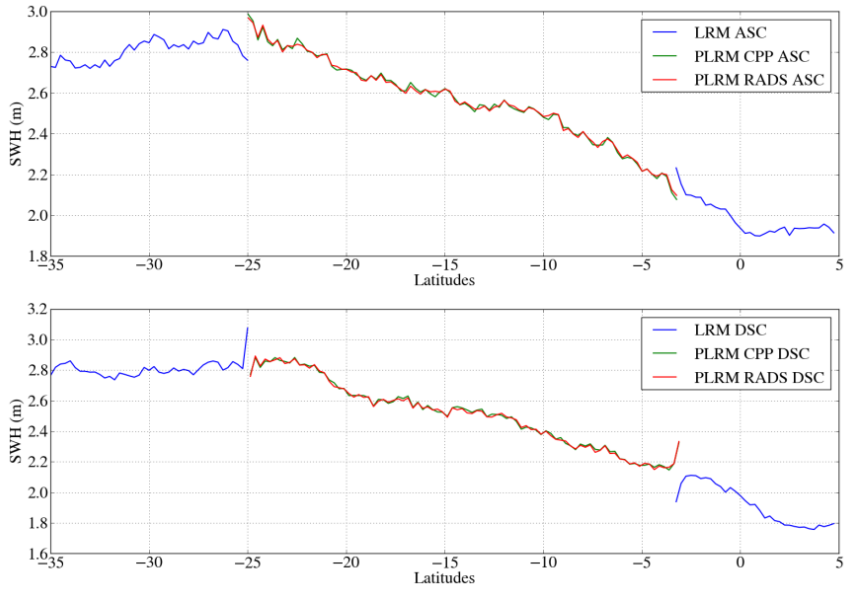

Figure 32: Mean SWH as function of band of latitudes for the TUDelft solution (in red), the V14 CPP dataset (in green) and the CPP LRM (in blue) over two months (July 2012 and January 2013).

3.2. Comparison of backscatter coefficient estimates

The same analysis is done on backscatter coefficient (sigma0).

3.2.1. Spectral analysis of sigma0

As was done for the other parameters, a spectral analysis has been performed on sigma0 estimates from both RDSAR solutions (Figure 33) showing two spectra well overlapped with each other and no differences between sigma0 noise levels. This result indicates very similar behaviour of the two RDSAR processing schemes on geophysical signals from high to low wavelengths.

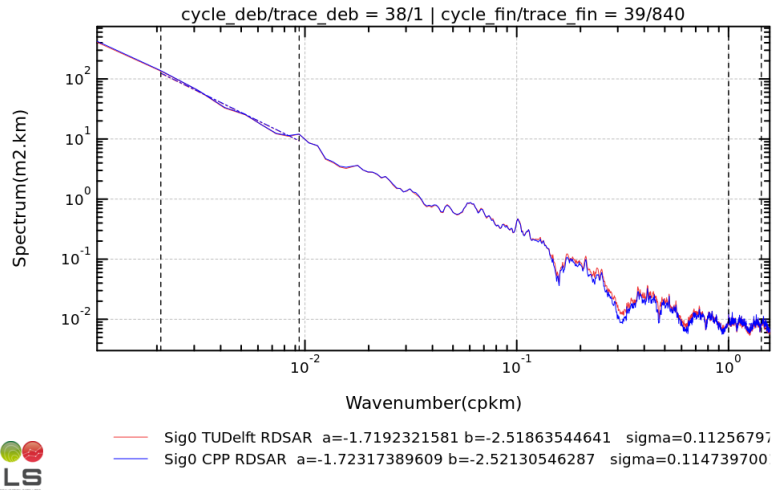

Figure 33: Mean sigma0 spectrum for V13 CPP (in blue) and TUDelft solution (in red) in January 2013 over the entire SAR-mode area.

3.2.2. **Sigma0 Histogram**

Figure 34 shows very similar sigma0 histograms after adjusting to Jason-2 Sigma-0. We also notice that the difference of sigma0 between ascending and descending passes is low, around 0.2dB for both the TuDelft RDSAR solution and the V13 CPP one.

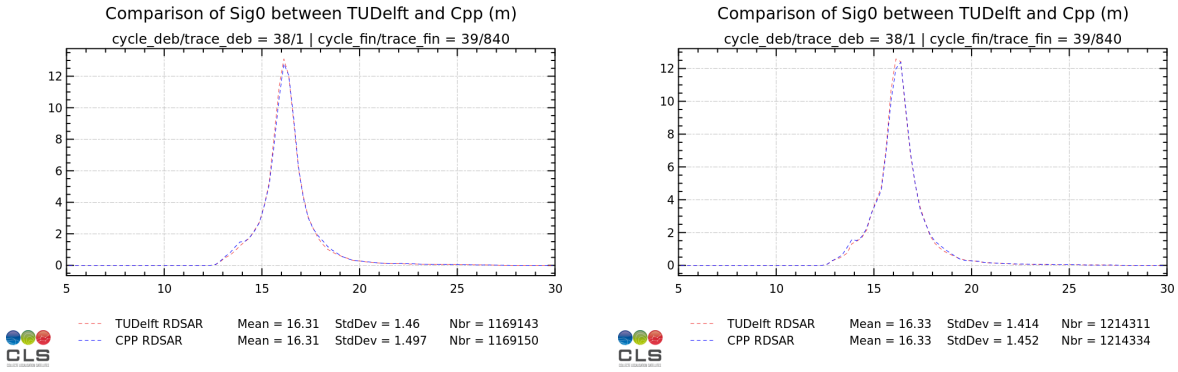

Figure 34: Histogram of 20-Hz Sigma0 from TUDelft RDSAR solution and V13 CPP in January 2013 for ascending (left panel) and descending (right panel) passes.

3.2.3. **Dependencies between parameters**

In Figure 35, the 20-Hz sigma0 residual between TUDelft and V13 CPP RDSAR solutions is plotted as function of SWH. Their difference varies slightly with the wave height, and may be as high as ±0.1dB at 2m SWH. These differences are low enough to consider this a quite good agreement between sigma0 estimates.

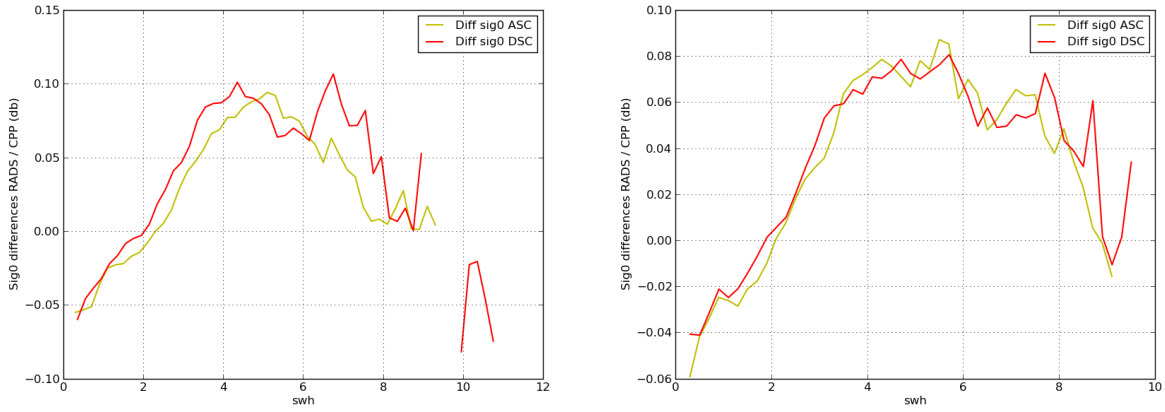

Figure 35: Dependencies of 20-Hz sigma0 residual with filtered SWH, in July 2012 and January 2013.

Figure 36 plots the sigma0 residual as function of the radial velocity and filtered wave height. In addition to the dependency to the wave height, the sigma0 residual appears to be also slightly correlated to the radial velocity, but at an extent that can also be neglected. Further investigation extended to a much larger time period would help to draw more reliable conclusions.

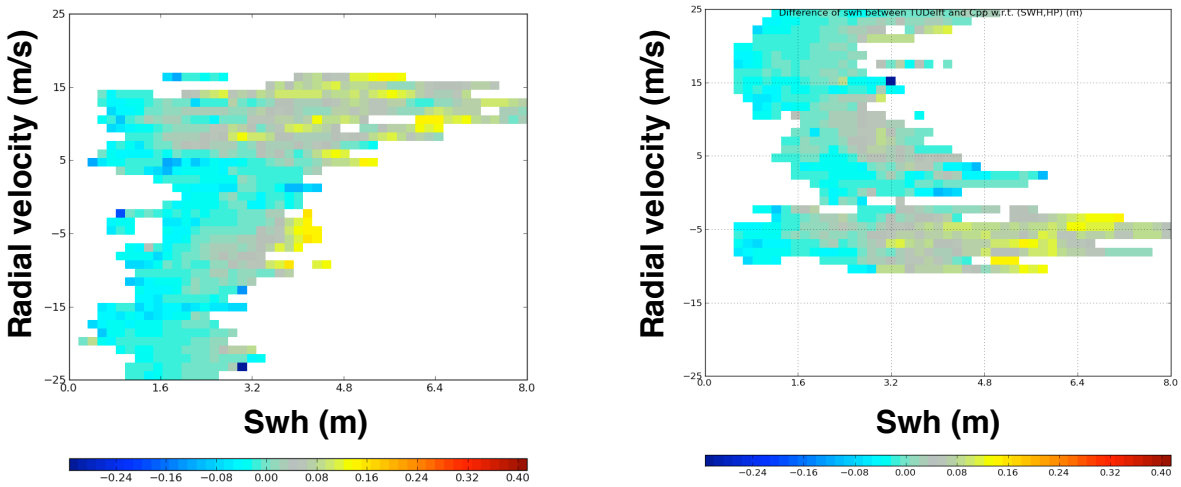

Figure 36: Dependencies of 20-Hz sigma0 residual (in dB unit) with filtered SWH and radial velocity in January 2013 for ascending (left panel) and descending (right panel) passes.

3.2.4. Sigma0 cartography

A map of differences between sigma0 computed from the TUDelft solution and the V13 CPP one confirms the preceding results. The sigma0 residual plotted in Figure 37 (top panel) by 2°x2° geographical bins shows slight dependency with wave heights (bottom panel) and possible correlation with the radial velocity (masked by stronger correlation with wave height).

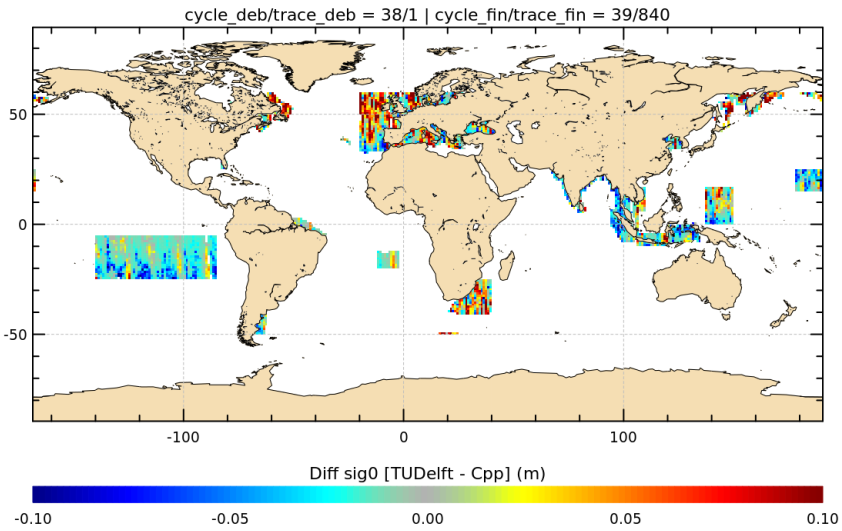

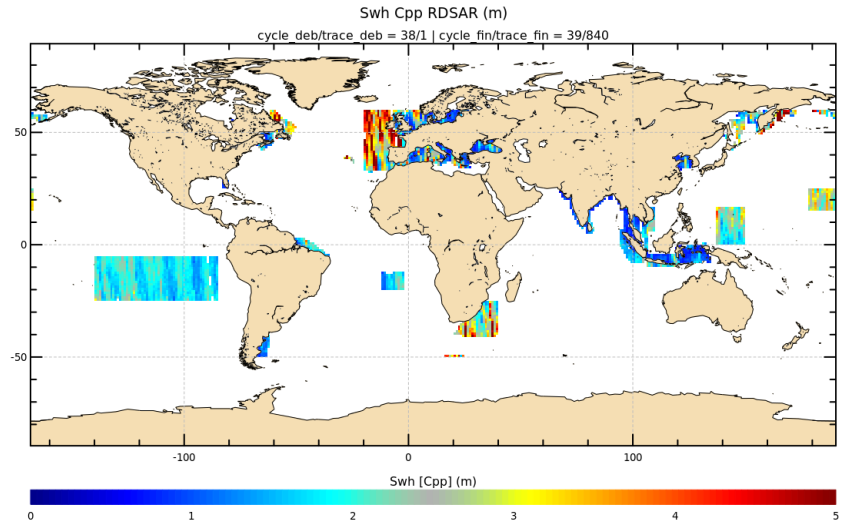

Figure 37: Difference of sigma0 from TUDelft RDSAR solution and CPP (top panel), and maps of SWH differences, in January 2013 for ascending passes.

3.2.5. Sigma0 continuity over the Pacific box with the V14 CPP solution

The analysis is done over the patch of the Equatorial Pacific over July 2012 and January 2013, separating between ascending and descending satellite passes.

The Figure 38 shows the sigma0 profiles from different processing as function of band of latitudes. The two RDSAR solutions (TUDelft and V14 CPP) show very comparable behaviour. We can also observe a quite seamless transition between LRM and RDSAR processing at -25° and -3°.

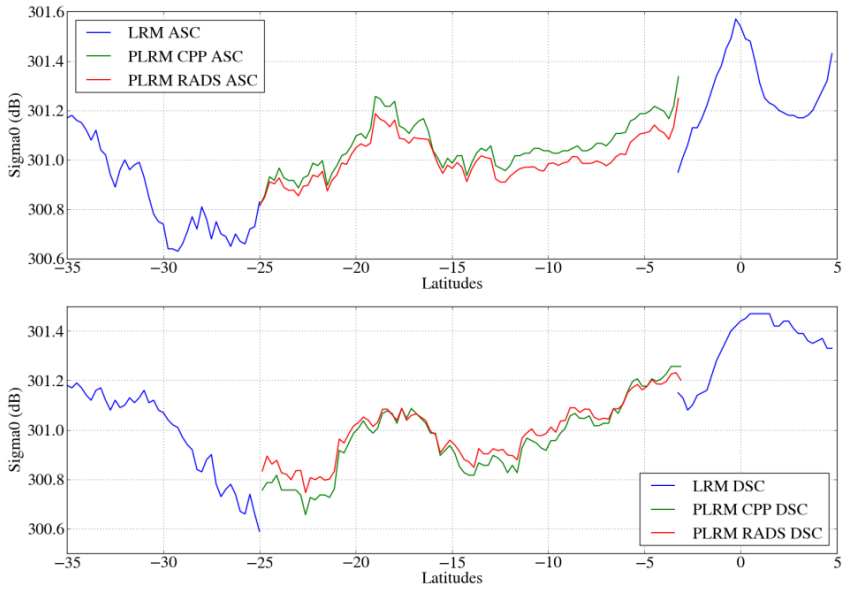

Figure 38: Mean sigma0 as function of band of latitudes for the TUDelft solution (in red), the V14 CPP dataset (in green) and the CPP LRM (in blue) over two months (July 2012 and January 2013).

3.1. Comparison of the mispointing angle estimates

The comparison between square-mispointing angle (ksi2) estimates is presented in this section.

The Figure 39 is the map of differences between ksi2 computed from the TUDelft solution and the V13 CPP one for ascending and descending passes in January 2013. From this figure, we can observe that these differences are not negligible, spanning from -0.08° to 0.06°.

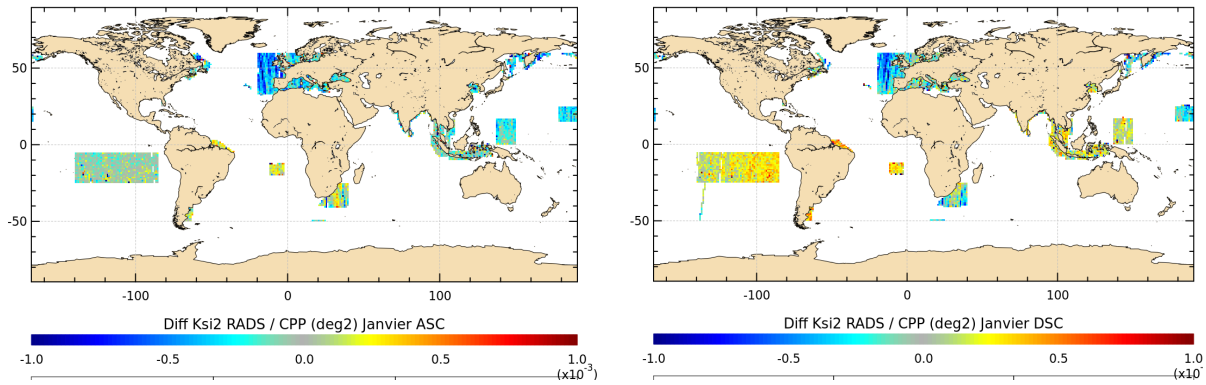

Figure 39: Mean map of difference of square-mispointing angle from TUDelft RDSAR solution and v13 CPP for ascending (left panel) and descending passes (right panel) in January 2013.

The differences between the two RDSAR solution products have been also analyzed in term of continuity over the patch of the Equatorial Pacific, over two months (July 2012 and January 2013). The Figure 40 shows the squared mispointing angle profiles from LRM and RDSAR processing at both transitions.

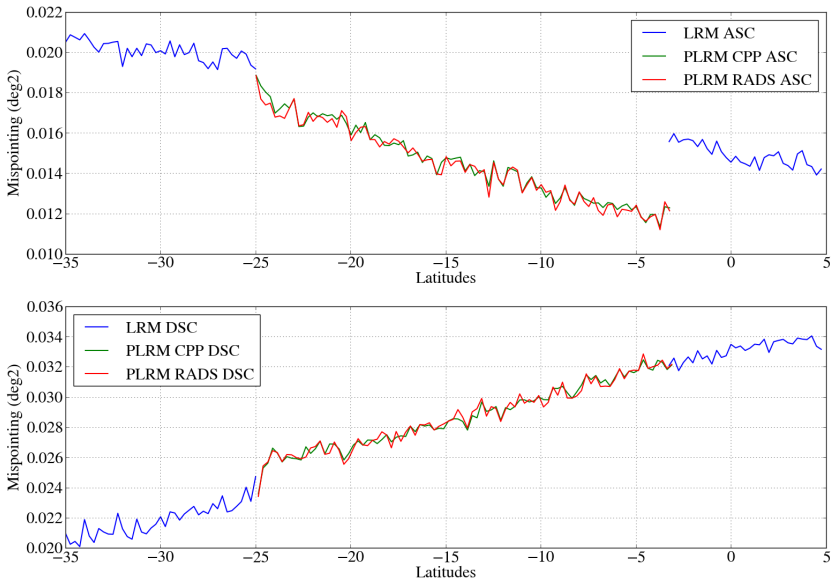

Figure 40: Mean square-mispointing angle as function of band of latitudes for the TUDelft solution (in red), the V13 CPP dataset (in green) and the CPP LRM (in blue) over July 2012 and January 2013.

First we can see very similar curves between both RDSAR solutions. This figure also shows an excellent agreement for descending tracks exhibiting almost no discontinuity at transitions. In other hand, the ascending tracks do not match as well. This bias is quite appreciable (with a 0.06° discontinuity at -3°) and has found to be correlated only with the orbital altitude of the satellite (anomaly due to imprecise values of altitude in the V13 CPP MLE4 retracker that was lately corrected in the v14 CPP). Once the correction applied, the curves do not show any noticeable residual discontinuity between LRM and V14 CPP RDSAR over both transitions (see in Figure 41), whereas the mispointing angles estimated from TUDelft RDSAR echo waveforms (with the imprecise MLE4 retracker) still appears to be low compared to LRM by 0.06°. A corrected MLE4 retracker would thus permit to obtain same ksi2 curves between the TUDelft RDSAR solution and the V14 CPP one.

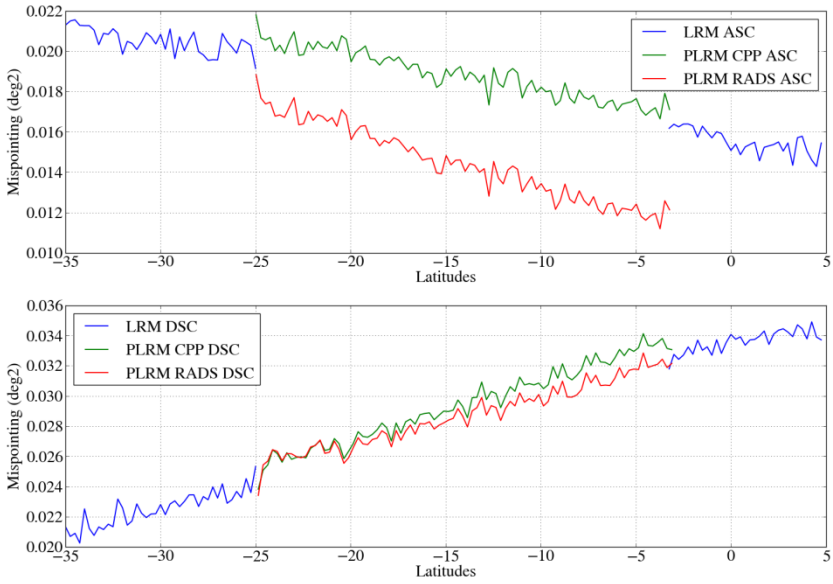

Figure 41: Mean square-mispointing angle as function of band of latitudes for the TUDelft solution (in red), the V14 CPP dataset (in green) and the CPP LRM (in blue) over two months (July 2012 and January 2013).

The retrieved mispointing angles from RDSAR processing are compared to the star trackers information to assess whether the two estimates are consistent or not. In Figure 42, the map shows the mean differences between ksi2 from the V14 CPP RDSAR solution and the squared off-axis angle of the antenna derived from the star trackers pointing measurements (contained in the V14 CPP products). From this map, we can see that the residuals for one month exhibit a quite appreciable mean value of 0.06°. We may question about the consistency of the antenna off-axis angles derived from star trackers measurements and notably the angular alignment computed between the star tracker boresight and the altimeter electromagnetic axis (performed with LRM data sets from preceding CPP version).

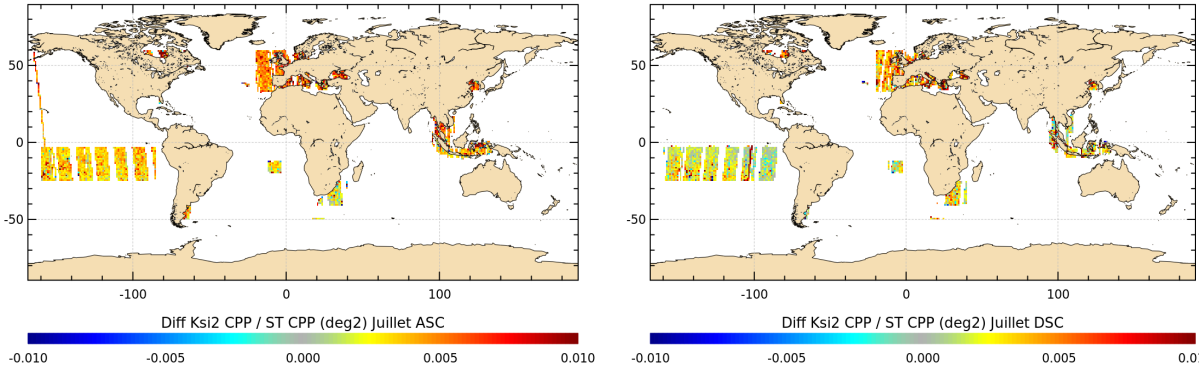

Figure 42: Mean map of difference of squared antenna-mispointing angle from V14 CPP product and the star trackers for ascending (left panel) and descending passes (right panel) in July 2012.

4. Conclusion

The objective of this study was to assess the TUDelft RDSAR method in comparison with the CPP one. To make this assessment meaningful, a same MLE4 ocean retracker was applied to waveforms of the two solutions (TUDelft and V13 CPP) and then the retrievals were analysed and compared.

Results of this study show that the residuals (for all parameters) are more or less correlated to the significant waveheight and that SLA differences are found to be also dependent on the radial velocity (partly due to the different time tag bias correction approach accounted for the computation of the orbit fields and also due to the difference in the alignment echoes processing). Differences of few cm in SLA, ten of cm in wave height and one tenth of dB in sigma0 are reported.

This assessment has been performed considering the V13 CPP products that served initially as inputs of the CP4O project. Afterwards, the CPP processing has been updated implementing the correction from the one-gate shifted waveform error. A very recent study has also been conducted to evaluate the retrieval differences with the last CPP version. And it seems to have no more dependency on SWH in the residuals between the TUDelft and V14 CPP RDSAR solutions, leading to SWH data sets from the two RDSAR solutions with quite close behaviour and similar performances.

On the other hand, a ~-540 us error in the time tag bias has been found on the TUDelft RDSAR data. Once this error is corrected, a remarkable agreement is obtained between both RDSAR solutions. An assessment of the TUDelft RDSAR solution in comparison with the V14 CPP one over more than the 2-month period of time, would permit to better precise the remaining differences.

After circulating earlier versions of this report, is was established that the RADS RDSAR data are indeed affected by a timing bias. The 400 µs that was added to the RDSAR time tags in RADS was based on analysis of LRM data. It now appears that this correction should not be applied to SAR mode data. The RADS RDSAR data produced in the framework of the CP4O project have since been corrected: 400 µs were removed from the time tags, the orbits were re-interpolated, and the sea level anomalies updated. This brings the time tags of the CPP v14 and RADS RDSAR data in a better agreement.

The residual ~140 µs timing bias between solutions couldn't be attributed to either side. Very recent crossover analyses also found somewhat same time tag bias for the two RDSAR data sets. We obviously reached the limit of our capacity (from different diagnostics) to determine more accurate time tag bias than 200 µs. At this level of accuracy, we can conclude that both solutions are very consistent.

5. References

[Boy and Moreau, 2013]: F. Boy and T. Moreau, "*Algorithm Theoretical Basis Document (ATBD) of the CPP RDSAR processing for oceans*", CNES report, S3A-NT-SRAL-00098-CNES, June 15, 2013.

[Labroue et al., 2014]: S. Labroue, M. Raynal and T. Moreau, "*Validation report: WP5000 assessment of CPP PLRM retracking*", CLS-DOS-NT-14-114, WP5000 CP4O report, June 20, 2014.

[Labroue et al., 2014]: S. Labroue, M. Raynal and T. Moreau, "*Validation report: WP5000 assessment of CPP SAR retracking*", CLS-DOS-NT-14-113, WP5000 CP4O report, June 20, 2014.

[Moreau et al., 2013]: T. Moreau, F. Boy and M. Raynal, "*Product Validation Report (PVR) of the CPP RDSAR processing for oceans*", CLS-DOS-NT-13-155, WP4000 CP4O report, June 18, 2013.

[Scharroo et al., 2013]: R. Scharroo, W. Smith, E. Leuliette, J. Lillibridge, "*The performance of CryoSat as an Ocean altimeter",* presentation at the Cryosat third user workshop, Dresden (Germany), March 12-14, 2013.

[Scharroo, 2014]: R. Scharroo, "*RADS RDSAR Algorithm Theoretical Basis Document (ATBD)",* WP4000 CP4O report, Version 0.3, August 1, 2014.